EXPERIMENTAL AND COMPUTATIONAL STUDY OF MIXING BEHAVIOR IN STIRRED TANKS EQUIPPED WITH SIDE-ENTRY IMPELLERS

by

JAIME ALBERTO SOSSA

B.Sc., UNIVERSIDAD INDUSTRIAL DE SANTANDER, COLOMBIA, 2007

A THESIS SUBMITED IN PARTIAL FULFILLMENT OF THE REQUIREMENTS FOR THE DEGREE OF

MASTER OF APPLIED SCIENCE

in

THE FACULTY OF GRADUATE STUDIES

(CHEMICAL AND BIOLOGICAL ENGINEERING)

THE UNIVERSITY OF BRITISH COLUMBIA

(Vancouver)

April 2012

Abstract

The wide applicability of mechanically stirred tanks in industry demands a comprehensive understanding of the physical and chemical phenomena controlling the performance of these fundamental units. The rheological complexity of some industrial fluids can create unfavorable mixing environments like dead zones that limit the contact area among the components being mixed. Also, the complex three dimensional nature of the flow generated by the impellers makes difficult the prediction of the flow properties, especially when the fluid viscosity is a function of the shear rate. Some research groups have investigated mixing flow of these kinds of fluids in conventional stirred tanks with top-entry impellers. But, little has been done to characterize the flow behavior in tanks with side-entry impellers.

In order to improve our understanding and provide insight into the flow mixing occurring in stirred tanks with side entry impellers, the flow field generated by different impellers in scale-down vessels filled with glycerine and carbopol solutions, was studied using the flow visualization technique, particle image velocimetry (PIV). Moreover, a computational model was built to predict flow variables and mixing characteristics unattainable with the experimental technique. The capabilities of the model were evaluated based on the velocity fields obtained experimentally. Good agreement was found between the predicted and measured macroscale flow structures and global mixing parameters. However, the models were unable to predict the symmetric flow observed during the experiments at high rotational speeds, likely due to the approach taken to simulate the flow, which provides a steady state velocity profile for one specific impeller location

Overall the results showed the formation of dead zones and segregated regions when mixing the non-Newtonian solutions. The size of the dynamic regions and the average velocity near the impeller were improved by increasing the suction area. Likewise, large pitch ratios were found to enhance the active mixing zone and the axial discharge. While, radial discharge and a strong tangential flow arose when the viscous forces dominate the flow. In conclusion, the flow features were defined by the Reynolds number in the vicinity of the impeller and the restrictions imposed by the walls of the vessel.

Preface

Parts of the sections 1.1, 1.3 and 2.1 along with chapter 4 have been submitted for publication: Sossa-Echeverria J. and Taghipour F., 2012. Effect of mixer geometry and operating conditions on flow mixing of shear thinning fluids with yield stress. I conducted all the experiments. The written work was a collaborative effort between my supervisor Prof. Fariborz Taghipour and me.

Parts of the sections 1.2, 2.2 and 2.3 along with chapter 3 have been submitted for publication: Sossa-Echeverria J. and Taghipour F., 2012. Mixing of Newtonian and Non-Newtonian fluids in a cylindrical mixer equipped with a side-entry impeller. I conducted all the experiments. The written work was a collaborative effort between my supervisor Prof. Fariborz Taghipour and me.

A version of chapter 5 has been submitted for publication: Sossa-Echeverria J. and Taghipour F., 2012. CFD study of mixing flow of non-Newtonian fluids in a stirred tank equipped with a side-entry impeller. I conducted all the experiments and all the CFD simulations. The written work was a collaborative effort between my supervisor Prof. Fariborz Taghipour and me.

Table of Contents

List of Tables

List of Figures

Nomenclature

D	Impeller diameter, cm
$\bar{\bar{D}}$	Strain rate tensor
E	Impeller clearance from the side wall, cm
F_A	Axial thrust, N
$\vec{F}$	External body forces, N
H	Liquid level, cm
k	Consistency index, Pa s
K_s	Metzner and Otto impeller constant
l	Mixing vessel length, cm
L_b	Vane length, m
L	Total velocity, m/s
L^*	Normalized total velocity
M	Torque, N m
n	Flow index
N	Rotational speed, rpm
N_p	Power number
N_q	Pumping number
N_f	Axial force number
p	Static pressure, Pa
P	Power, watt
Q	Flow rate, m^3/s
r	Position vector in the rotating frame
R_b	Vane radius, m
Re	Reynolds number
Re_y	Yield stress Reynolds number
T	Diameter of cylindrical tank, cm
U_{tip}	Tip speed, m/s
U	Axial velocity, m/s
U^*	Normalized axial velocity
V	Vertical velocity, m/s
V^*	Normalized vertical velocity
$v_{\dot{\gamma}}$	Volume of a fluid element with shear rate $\dot{\gamma}$, m^3

V_c Cavern volume, m^3

$\vec{v}$ Absolute velocity, m/s

$\vec{v}_r$ Relative velocity, m/s

W Mixing vessel width, cm

X axial distance in front of the impeller, mm

X^* X/D

Y Vertical distance from impeller center, mm

Y^* Y/D

Z Radial position from the impeller center, cm

Z_l Laser sheet thickness, mm

Greek letters

Δt Inter image time, s

ρ Fluid density, Kg/m^3

Ω Angular velocity, rad/s

$\vec{\Omega}$ Angular velocity vector

η Viscosity, Pa·s

τ Shear stress, Pa

$\bar{\bar{\tau}}$ Stress tensor

$\dot{\gamma}$ Shear rate, s^{-1}

τ_y Yield stress, Pa

Acknowledgments

I would like to express my sincere gratitude to my supervisor Prof. Fariborz Taghipour for his invaluable support throughout my graduate experience. I will always be grateful for his guidance, patience, motivation, knowledge and enthusiasm. Special thanks to Prof. Chad Bennington and Clara Gomez for believing in me and helping me to study in this outstanding university.

I would like to thank Prof. Savvas Hatzikiriakos and Prof. James Feng for taking time out of their schedules to be part of my defense committee. I also thank the faculty, staff and my fellow students in the CHBE department and the Pulp and Paper Center.

I thank my good friends Masita, Francisco and Xinmei for making the room 227 in the Pulp and Paper Center the best place to work. Thanks to them for their help, advice and positive energy.

There are not words to show my everlasting gratitude and appreciation to my parents, Orlando and Yolanda, my brothers, Carolina and Julian, and my future wife Paula for their unconditional love and support. Last but not least, thanks to God for giving me the opportunity to live this fantastic journey called life.

1. Introduction

It has been documented that the cost of poor mixing in a large chemical company could be as high as $100 million per year (Paul et al., 2004). Mixing play a key role in a wide range of industries, including pharmaceuticals, petrochemicals, biotechnology, polymer processing, food, mineral processing, waste water and pulp and paper among others. Failure to provide efficient mixing in the manufacturing processes of these industries can cause low quality products, longer processing times, waste of raw materials, safety issues and yield losses in general. The significant impact of mixing problems on the operating costs of any process and the economical benefits derived from any improved mixing technology are a clear motivation to perform research on this main unit operation.

The purpose of mixing is to reduce inhomogeneities of concentration, phase or temperature. One of the most common devices to perform this task is the stirred tank. A thorough understanding of the operation of these equipments requires the analysis of a large number of aspects including mechanical properties, process characteristics, and physical and chemical phenomena at different scales.

The rationale of this study is to provide some macro-scale insights from the fluid dynamic perspective. Some of the aspects affecting the hydrodynamic of the stirred tanks are rheological properties of the fluids, geometrical characteristics of the mixing device and operating conditions. For simple low viscous-Newtonian fluids, there is a comprehensive set of studies on the flow structures and the mixing mechanisms for different mixing conditions. However, a large portion of the fluids present in industry either are high viscous fluids or exhibit complex rheologies like shear thinning behaviour (characterized by a negative correlation between the viscosity and the shear rate) and yield stress (stress at which the material begins to deform plastically). Mixing of these kind of fluids can demand specific levels of shear rate, or can generate undesired mixing conditions like dead zones (green region in Figure 1-1). Thus, the design, optimization and scale-up of mixing systems for fluids with complex rheologies require a complete characterization of the flow structures and the fluid properties in the active zones (orange region in Figure 1-1).

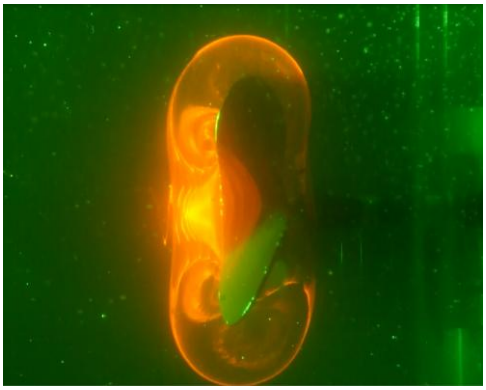

Figure 1-1. Illustration of active (orange region) and dead (green region) zones, when mixing fluids with yield stress.

Most of the studies describing flow mixing inside stirred tanks are focused on mixing tanks with top entry impellers (Figure 1-2a), and very scarce information is available in the open literature for tanks with side-entry impellers (Figure 1-2b). This configuration has been actively used in pulp and paper applications, as well as in blending and sludge control in oil tanks. Recently, side-entry impellers have gained popularity in other industries due to the particular benefits that they offer. Some of these benefits include asymmetric flow, lower initial cost and smaller shaft lengths in tall tanks (Bakker and Gates, 1995; Hemrajani and Tatterson, 2004). Accordingly, the present study was meant to examine the flow structures generated in stirred tanks equipped with side entry impellers and filled with viscous and pseudoplastic fluids with yield stress. The hydrodynamics was investigated by means of experimental flow visualization and computational modeling. Particle image velocimetry was the experimental technique used to obtain two-dimensional velocity maps at different locations inside the mixing domain. This technique measures the displacement of tracer particles added to the fluid to obtain instantaneous velocity fields. On the other hand, a three dimensional representation of the steady-state flow was created using computational fluid dynamics. The computational model solves the mass and momentum balance equations applied to the mixing domain to give information on pressures, velocities and related properties.

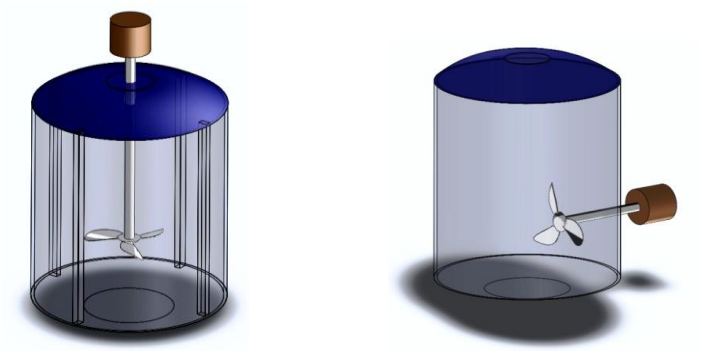

(a) (b)

Figure 1-2. (a) Top entry impeller, (b) Side entry impeller

1.1 Effect of geometrical properties of stirred tanks[1]

The proper design and optimization of stirred tanks requires a fundamental understanding of all the variables potentially affecting the performance of these essential units. Some of these variables include geometrical properties of the mixing equipment, such as vessel shape, impeller geometry, baffles, number of impellers and impeller clearance. The existing diversity of each of these parameters provides an enormous spectrum of possibilities to tackle any mixing necessity.

Impellers are usually classified by flow patterns, applications and special geometries. Generally speaking, there are two main flow patterns i.e. axial and radial flow (Figure 1-3). But, some deviations from these patterns might arise under specific conditions or especial impeller properties. Axial flow impellers are characterized by a single circulating loop and high pumping capacity. The shear levels generated by this kind of impeller might vary according to the blade characteristics. On the other hand, radial flow impellers produce two circulating loops, with some degree of segregation between them. The pumping capacity is lower compared to that of the axial flow impeller; but offers higher shear and turbulence levels. The selection of the most effective impeller for a given application depends on process requirements and operating restrictions. Examples of axial and radial impellers are presented in Figure 1-4

[1] Part of this section has been submitted for publication. **Sossa-Echeverria J. and Taghipour F., 2012. Effect of mixer geometry and operating conditions on flow mixing of shear thinning fluids with yield stress.**

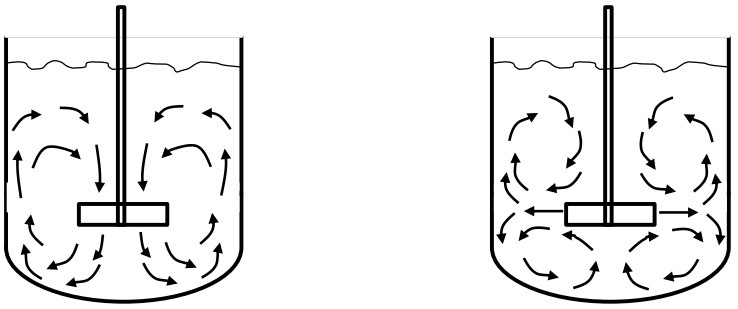

(a) (b)

Figure 1-3. (a) Axial flow, (b) Radial flow

A detailed description of impeller properties, flow patterns and applications can be found in Hemrajani and Tatterson, (2004).

(a) (b)

Figure 1-4. (a) Axial impeller, (b) Radial impeller

Previous studies have shown the effect of impeller design on mixing flow under different operating conditions. Axial flow impellers are characterized by both axial and radial flow discharge in the case of low to medium viscosities. Kelly and Gigas (2003) have shown that this discharge angle is strongly related to the Reynolds number (equation 1-1) in the laminar and transitional flow regimes.

$$Re = \frac{\rho N D^2}{\eta} \qquad 1\text{-}1$$

Geometrical characteristics of an impeller, to a great degree determine its performance. The pitch is defined as the distance a point on an impeller blade would move along the axis of rotation in one revolution of the impeller. A positive correlation has been determined between pitch ratio (ratio of the pitch to the impeller diameter) and other impeller properties like power number (N_p),

axial force number (N_f) and pumping number (N_q) for axial flow impellers as follows (Kumaresan and Joshi, 2006; Bhole and Bennington, 2009).

$$N_p = \frac{P}{\rho N^3 D^5} \quad 1\text{-}2$$

$$N_f = \frac{F_A}{\rho N^2 D^4} \quad 1\text{-}3$$

$$N_q = \frac{Q}{N D^3} \quad 1\text{-}4$$

The Power number (parameter that represents the power requirements) can be reduced by keeping a nearly constant pitch across the blade i.e. using hydrofoil impellers (Hemrajani and Tatterson, 2004). The hydrofoil impellers offer lower shear compared to conventional axial flow impellers and are suitable for mixing yield stress fluids (Bhole et al., 2009). Another important parameter, affecting power consumption and flow pattern is the impeller location. There are some guidelines in literature for impeller clearance (distance between the impeller and vessel rear wall) based on empirical work (Yackel, 1990; Bhole et al., 2011). However their applicability might be limited to specific conditions, since the optimum dimensionless clearance *E/D* (where *E* is clearance from rear-wall, and *D* is impeller diameter) is a function of operating conditions, rheology, and mechanical constraints. Bhole et al., (2011) used electrical resistance tomography to identify dead zones inside a stock chest and showed that for a 3% hardwood pulp suspension the optimal *E/D* ratio is close to 0.5. Moreover, they found a substantial restriction of the flow to the impeller suction at *E/D*=0.14, which leads to an increase of the power requirements.

Besides impeller characteristics and location, the vessel shape can be a key variable when designing mixing systems. The most common configuration for stirred tanks is the cylindrical vessel equipped with top entry impellers, which performance is well described in literature. Other nonconventional arrangements are cylindrical and rectangular vessels equipped with side entry impellers. These systems are used in industrial processes such as waste water treatment and agitation of pulp fiber suspensions among others (Bhole et al., 2009). Gomez et al., (2010) reported characteristic flow structures of a viscous Newtonian fluid in a rectangular vessel equipped with a side entry impeller. This study shows flow patterns characteristic of radial

impellers, and recirculation loops generated by the strike of the impeller discharge to the bottom of the vessel. It is also shown how this bottom wall drives secondary flows in the axial direction.

1.2 Mixing of Newtonian and non-Newtonian fluids[2]

The close relationship between viscosity and flow regime, suggests that rheological properties define in a good extent mixing variables such as blending time, flow pattern, power consumption. Turbulence dramatically affects any physical and chemical phenomena occurring in any mixing process. Due to the time-dependency of the turbulent flow, nonlinear inertial forces dominate the flow, and there is a permanent reorientation of fluid particles. This enhances the mixing quality and avoids the formation of segregated regions (Lamberto et al., 1996; Kresta and Brodkey, 2004). However, turbulent flow regime is not suitable or attainable in all processes. Systems where turbulence can be harmful to the fluid or high viscosities are present, the mixing process has to be performed in laminar regime. Pulp suspensions, polymers, food, paint, greases, drugs, drilling mud are some examples of industries, where mixing devices operate in the laminar regime.

It has been established that good mixing can be obtained in the laminar regimen when the flow is governed by chaotic motion (Szalai et al., 2004). Chaotic flow is described by an exponential rate of stretching and folding, which substitutes the effect of time-dependency in turbulent mixing. The chaotic flow in the laminar regime can be identified using Lagrangian analysis as presented by Lamberto et al., (2001). In this study, regular (segregated zones from the bulk flow) and chaotic regions were studied using a Lagrangian approach. Before implementing this Lagrangian analysis, it is necessary to obtain information about circulation loops, velocity profiles and flow patterns in the mixing domain. Hence, several studies have used Eulerian approaches to globally describe the flow structures and the fluid dynamics of different mixing configurations. Lamberto et al., (1999) showed bulk flow patterns of a 6-blade radial flow impeller under different Reynolds numbers. In all cases, radial discharge and segregated regions were found above and below the impeller. The mass transfer between the bulk flow and the segregated regions was found to be limited to diffusion, which decreases the mixing performance. The position of the segregated zones was found to be a function of the Reynolds

[2] Part of this section has been submitted for publication. **Sossa-Echeverria J. and Taghipour F., 2012. Mixing of Newtonian and Non-Newtonian fluids in a cylindrical mixer equipped with a side-entry impeller.**

number. The mixing efficiency of these systems can be improved by using a time-dependent rotational speed that disrupts the segregated zones (Lamberto et al., 1999). Bakker et al., (1996) investigated the radial discharge generated by a pitched blade turbine. The flow was mainly tangential and was limited to the region near the impeller. Similar flow characteristics were found by Gomez et al., (2010), when studying mixing of a viscous fluid in a rectangular tank equipped with a side entry axial impeller. In the mentioned work, the macro-scale flow structures revealed the four circulation loops characteristic of radial discharge. This unexpected pattern is a consequence of the high viscosity of the fluid.

Complex rheological properties can significantly affect the mixing conditions. Thus, a number of studies have been dedicated to mixing of non-Newtonian fluids, mainly shear thinning fluids which are very common in industrial processes. The mixing dynamic displayed by these fluids is governed by several variables, i.e. impeller and tank geometry, rotational speed, rheology and the distribution of mechanical components inside the tank (Kelly and Gigas 2003; Arratia et al., 2006; Annearchard et al., 2006; Thakur et al., 2004). The flow for axial flow impellers as mentioned before is characterized by an outward pumping action in the axial direction at high angular velocities (Jaworski et al., 1996). As the impeller speed decreases or the fluid viscosity increases, the flow around the impeller reorganizes and adopts a dominant radial flow, which might affect the impeller performance (Couerbe et al., 2008). The mixing performance can be evaluated by thorough visualization of the dynamic regions. Arratia et al., (2006) presented a detailed description of the flow pattern generated by a Rushton impeller in a shear-thinning fluid, and highlighted recirculation loops surrounding the impeller. The main ingredients of chaotic flow were recognized in specific regions, and it was shown how the stretching values and the chaotic regions increase with the Reynolds number. Other important findings were compartmentalization of the flow and segregated zones from the bulk flow.

The formation of active zones (known as caverns) around the impeller and dead zones away from it have been reported when mixing fluids with yield stress. The limit of the cavern can be defined as the surface where the local shear stress balances the fluid yield stress. The size of the cavern has been found to be a function of the rotational speed and the rheological parameters (Pakzad et al., 2008; Arratia et al., 2006; Amanullah et al., 1998; Wilkens et al., 2005). However, there is not a single mathematical expression (based on merely fundamental concepts) in the open literature able to relate cavern size and shape with mixing conditions. Electrical Resistance

Tomography (ERT) and other visualization techniques have been used to study the formation of these caverns for different fluids (Elson et al., 1986; Arratia et al. 2006; Pakzad et al., 2008; Hui et al., 2009; Bhole and Bennington, 2010; Bhole et al., 2011). The reported results show significant differences on cavern characteristics. Hence, a wide variety of expressions based on force balances and cavern shape have been developed to estimate cavern size (Elson et al., 1986; Amanullah et al., 1998; Adams and Barigou, 2007). These expressions are applicable only under certain conditions. Furthermore, the values of some mixing variables need to be known for their implementation. These variables include the power number and axial force number (dimensionless number of axial thrust) at the operating Reynolds number, or the velocity at the cavern boundary (Adams and Barigou, 2007). This information might be hard to obtain, since the shear thinning behaviour makes the estimation of the Reynolds number difficult. The viscosity included in the Reynolds number (Equation 1-1), can be obtained using the expression proposed by Metzner and Otto ($\dot{\gamma} = K_s N$) along with a rheology model. Although, this expression has been successfully proved at low Reynolds numbers (Re < 30) (Metzner and Otto, 1957; Thakur et al., 2004), its implementation has been found to under-predict the actual Reynolds number at higher Reynolds numbers (Kelly and Gigas, 2003).

1.3 Particle image velocimetry (PIV)[3]

Different experimental techniques are applied to study mixing dynamics. Particle image velocimetry (PIV) is a powerful technique to obtain meaningful data about the flow field at specific positions inside the mixing domain. Unlike other non-intrusive visualization techniques like particle tracking velocimetry (PTV) and laser doppler velocimetry **(**LDV), PIV provides high density velocity fields in a defined grid, which may reveal circulation flow patterns and velocity gradients (Adrian, 1991). The velocity fields obtained from this visualization technique are also commonly used to evaluate capabilities of computational models as presented by Couerbe et al., (2008), Arratia et al., (2006), Khopkar et al., (2004), Torre et al., (2007) and Shen et al., (1998).

[3] Part of this section has been submitted for publication. **Sossa-Echeverria J. and Taghipour F., 2012. Effect of mixer geometry and operating conditions on flow mixing of shear thinning fluids with yield stress.**

PIV extracts instantaneous local velocities and flow characteristics by measuring the displacement of small suspended tracer particles in a known time interval. The distance is measured from two consecutive photos of the particles, and the resolution of the vector fields is given by the size of the elements of an arbitrary grid applied to the photos. The time between photos depends on the time scales in the flow, and is used to calculate the velocity. The displacements of the particles enclosed in each cell (known as interrogation window) of the grid are analyzed and correlated to report one velocity vector per cell. The particle properties have to be carefully selected so that they follow the fluid trajectories and do not alter the flow properties. The ability of the particles to track the flow can be estimated from the Stokes' drag law (Melling, 1997)

The basic components of a PIV system are shown in Figure (1-5). The camera (located perpendicular to the light sheet) has to capture two consecutive image frames of the flow field at the same time the laser emits two pulsed light sheets. The interrogation windows of the pair of images are then processed by an image processing software to obtain the vector map. The displacement information is obtained through cross-correlation techniques that detect the location of the highest correlation peak in each interrogation window. That is, the correlation finds the best pattern match between the particles of the corresponding interrogation windows of the two image frames. Digital filters can be applied prior to computation of the correlations peaks in order to improve the results. The displacement derived from the correlation is divided by the time between pulses to calculate the velocity. An elaborate description of this technique can be found in Adrian (1991), Prasad (2000) and Mckenna and Mcgillis (2002).

PIV is an optically-based visualization technique and its implementation demands the use of transparent fluids so that the tracer particles can be seen through the flow. Aqueous carbopol solutions are transparent fluids, which are also able to mimic complex rheologies of some industrial fluids. One advantage of using carbopol solutions to simulate industrial fluids is that its rheological characterization can often be done more precisely than that of the industrial fluids. Those properties make carbopol solutions suitable for the development of this work. The appropriateness of carbopol solutions to perform PIV experiments have been shown in previous studies (Sheridan et al., 1996; Arratia et al., 2006; Couerbe et al., 2008; Tokpavi et al., 2009; Park and Liu, 2010), where the flow properties were evaluated for a wide range of flow systems. Some studies have shown the rheological properties of carbopol solutions and their similarities

with complex fluids found in industrial processes (Curran et al., 2002; Piau, 2007). A carbopol solution is a physical gel, composed of highly cross-linked polymer particles and generally speaking, it exhibits shear-thinning behaviour with yield stress (Roberts and Barnes, 2001). Although the concept of yield stress is controversial, it has been shown that it provides an appropriate way to describe the macroscale flow conditions under different shear rate values. Gomez et al., (2010) presented qualitative similarities of aqueous carbopol solutions and pulp suspensions, along with a set of conditions to mimic the mixing quality attained in a particular pulp suspension mixing system.

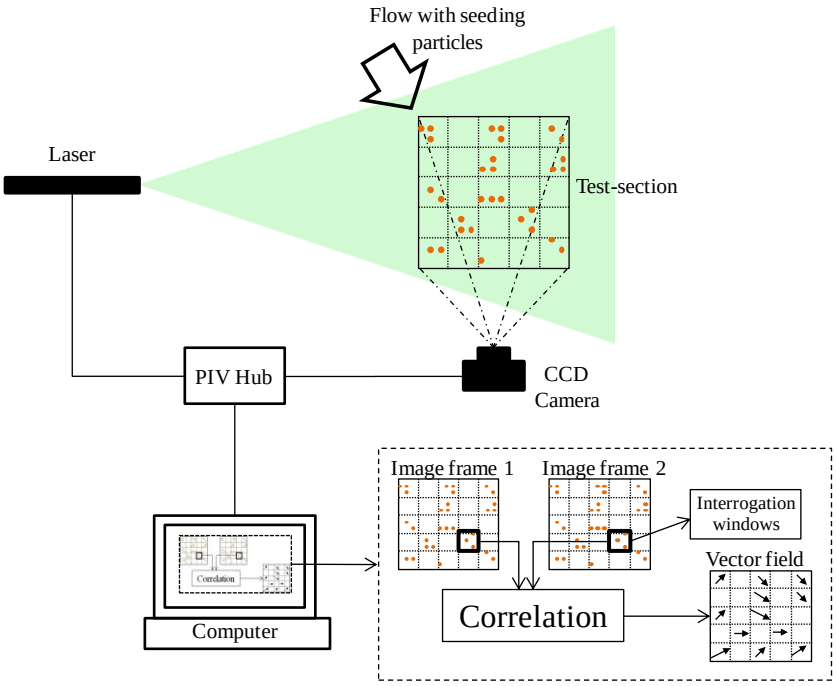

Figure 1-5. Operation of PIV system

1.4 Computational fluid dynamics (CFD)

Computational fluid dynamics (CFD) provides information on flow field variables, with details not usually available through experimentation. CFD uses numerical methods and algorithms to solve the governing equations of problems that involve fluid flows, including the mass and momentum conservation equations. In order to solve these equations, the flow region is divided into small cells (computational grid) so that the discretized form of the differential equations of momentum, energy and mass balance can be applied. A set of boundary conditions and

additional models (which depends on the application) need to be specified in order to solve these equations. The final array of equations is solved iteratively and the capability of the results to represent the real flow conditions highly depends on the quality of the grid, the numerical methods and the ending residuals between iterations. Information regarding the discretization and numerical solutions can be found in (Ford, 2004). The main flow variables are computed and stored at specific positions within the cells of the computational grid and can be post-processed to derive other flow properties.

CFD models of mechanically stirred tanks provide information on hydrodynamic variables and mixing parameters that would be costly or simply unfeasible to obtain with the existing experimental techniques. Some of the information offered by these models includes shear rates, energy dissipation, power requirements, mixing structures, pumping capacities, velocity fields and mixing times (Zalc et al., 2002; Kelly and Gigas, 2003; Kumaresan and Joshi, 2006; Ihejirika and Ein-Mozaffari, 2007 and Kelly and Humphrey, 1998). The fact of having rotating parts and elaborated geometries (impellers shapes) adds complexity to the application of CFD to model stirred tanks. The meshing process requires a special treatment in the proximity of the impeller so that the predicted flow structures reflect the effect of specific blade shapes. A higher mesh refinement near the impeller and advanced size functions have been used in some studies (Lamberto et al., 1999; Adams and Barigou, 2007; Gomez et al., 2010) to capture quantities with large gradients in the flow domain around the impeller. Different approaches are available to model the motion of the rotating impeller with respect to the stationary tank walls and baffles. A time average method can be implemented by replacing the rotating impeller with stationary boundary conditions that represent the impeller discharge. Information on velocity profiles (obtained from experimental data) or momentum sources can be used to symbolize the flow discharged by the impeller. This approach is the simplest way to model a stirred tank. However, it overlooks details of flow around the blades and requires an additional source of information.

The snapshot or frozen rotor approach does not need experimental data, and it can predict the effects of different blade shapes, since it involves the actual geometry of the impeller. However, it calculates the flow field for one impeller position only. This method solves the steady-state flow by modeling the fluid region that contains the impeller in a moving reference frame and the rest of the fluid in a stationary reference frame. The continuity and momentum equations in the region around the impeller are modified to account for the rotating frame as follows:

$$\nabla \cdot (\rho \vec{v}_r) = 0 \quad \text{1-5}$$

$$\nabla \cdot (\rho \vec{v}_r \vec{v}) + \rho\left(\vec{\Omega} \times \vec{v}\right) = -\nabla p + \nabla \cdot (\bar{\bar{\tau}}) + \vec{F} \quad \text{1-6}$$

Where ρ is the density, p is the static pressure, $\bar{\bar{\tau}}$ is the stress tensor, $\vec{\Omega}$ is the angular velocity vector, $\vec{F}$ represents the external body forces, $\vec{v}$ is the absolute velocity and $\vec{v}_r$ refers to the relative velocity, which is related to the absolute velocity as shown in equation 1-7. $\vec{r}$ is the position vector in the rotating frame.

$$\vec{v}_r = \vec{v} - \left(\vec{\Omega} \times \vec{r}\right) \quad \text{1-7}$$

The additional term ($\rho\left(\vec{\Omega} \times \vec{v}\right)$) in the right hand side of the momentum equation (equation 1-6) accounts for the additional acceleration experienced by the fluid in the rotating frame.

The moving reference frame method was used in this study, which implementation has been successfully proved in other studies with similar mixing configurations (Saeed et al., 2008; Pakzad et al., 2008; Gomez et al., 2010; Kelly and Gigas, 2003). Limitations of this approach might arise when the transient flow field generated by the interaction of the impeller and the vessel walls or baffles is important. Likewise, it is not suitable when the flow at the interface between moving and stationary zones is excessively complicated.

Unsteady methods should be implemented when transient flows are the primary interest. In those cases the impeller actually moves with respect to the stationary components of the tank, thereby obtaining a full time-dependant flow. This is the most rigorous and computationally expensive solution, since the mesh has to change with time and converged solutions for each time step are needed.

1.5 Research objectives

Considering the many benefits offered by stirred tanks equipped with side-entry impellers, and the lack of detailed information on their performance, the main goal of this work is:

- To present a broad study of the flow structures and relevant mixing variables inside cylindrical tanks equipped with side-entry impellers, operating in laminar and transitional flow regimes. The research was divided into three main topics with specific objectives as follows:

I. *Mixing behavior of Newtonian and Non-Newtonian fluids in a stirred tank equipped with a side-entry impeller.*

- To identify the effect of rheological properties on the flow characteristics and the impeller performance using a flow visualization technique (the flow structures of a viscous Newtonian fluid and three non-Newtonian fluids displaying shear thinning behaviour with yields stress are evaluated).

II. *Effect of mixer geometry and operating conditions on flow mixing of non-Newtonian fluids.*

- To investigate the flow pattern and some characteristic mixing parameters (pumping number and power number) generated under different geometrical and operating conditions using a flow visualization approach (three axial flow impellers, three impeller clearances, which is the distance from the rear wall to the impeller, and two vessel shapes are considered in this study).

III. *CFD study of mixing flow of Non-Newtonian fluids.*

- To develop a CFD model of a stirred tank equipped with a side-entry impeller, and to experimentally evaluate the model capabilities and limitations to predict the effect of geometrical and rheological properties.
- To obtain from the computational model information on mixing variables not derivable from the experimental results (some of the variables include segregated zones, three dimensional flow structures, shear rate distributions and cavern size and shape).

2. Experimental setup

2.1 PIV system[4]

A 2D-PIV system from Dantec Dynamics Inc. was used for measuring the flow field. The basic components of the experimental setup are presented in Figure 2-1. The system consists of: (1) a dual head Nd:YAG laser to illuminate the region of interest, (2) a high resolution (1344×1024 pixels) progressive-scan interline CCD camera (Hamamatsu, model HiSense MkII) to record the position of the tracer particles at two successive snapshots, (3) a triggering system composed of a proximity switch (Wenglor IB40) and an aluminum rod mounted on the impeller shaft (this system activates the photo acquisition system at specific positions of the impeller), (4) a PIV hub that controls the time between laser pulses and synchronizes the action of the trigger with the laser and the camera, (5) a personal computer that operates the PIV hub, stores photos and obtains velocity fields from cross-correlation techniques, (6) a 0.33 HP motor with a digital control of the motor speed, (7) a transparent plexiglass mixing vessel of approximately 0.03 m^3 containing the fluid which is uniformly seeded with tracer particles (these are PMMA-Rhodamine B particles with a size distribution of 20-50μm and density of 1.19 g/cm^3), (8) a rectangular plexiglass tank enclosing the mixing vessel. The external tank is filled with water and its purpose is to correct the optical distortion created by the curved surface of the cylindrical vessel.

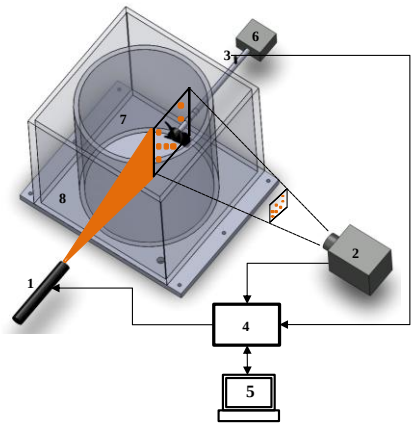

Figure 2-1. PIV experimental setup

[4] Part of this section has been submitted for publication. **Sossa-Echeverria J. and Taghipour F., 2012. Effect of mixer geometry and operating conditions on flow mixing of shear thinning fluids with yield stress.**

Two mixing tanks of cylindrical and rectangular shapes, with similar volumetric capacity were utilized. The dimensions of the cylindrical tank (Figure 2-2a) are diameter T=32.9 cm and height H=35 cm, whereas for the rectangular tank (Figure 2-2b) they are length l=36.5 cm, width W=24.5 cm and height H=35 cm. As shown in Figure 2-2, three different vertical planes (test-sections) inside the tanks were investigated, that is, one (#1) at the center of the impeller (Z=0 cm), another (#2) close to the blade tip (Z=5 cm) and one (#3) close to the tank wall (Z=8 cm). These planes are generated by aligning the light sheet created by the laser (with a thickness of approximately 2 mm) with the sought "Z" position and by framing, with the camera, the desired area around the impeller. The light refracted by the plane was filtered using a 570 nm filter at the camera lens, so that the light beams refracted by air bubbles was not recorded and only those from the particles were captured.

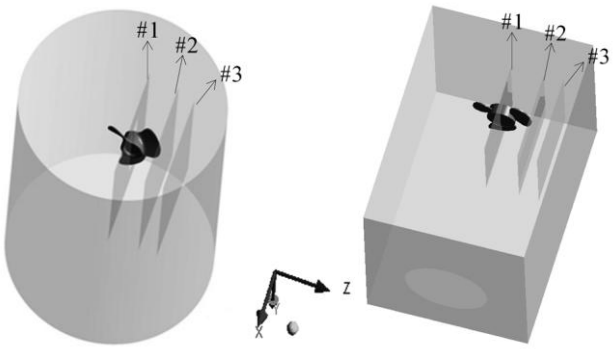

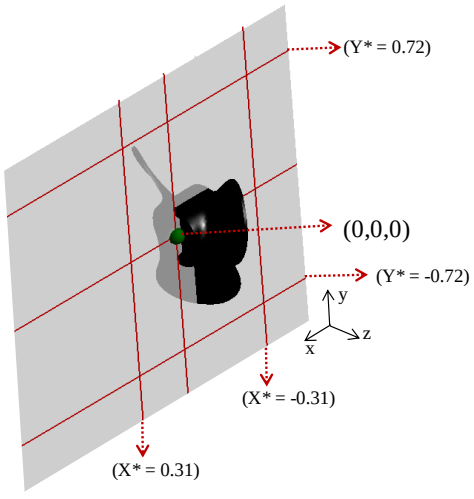

(c)

Figure 2-2. Mixing tanks and test sections (a) Cylindrical tank, (b) Rectangular tank, (c) Test section and sample lines for velocity profiles

The flow field of three impellers (Figure 2-3) with diameter *D*=9.652 cm was studied. These are 3 bladed, axial-flow hydrofoil impellers used at industrial level, in mixers with side-entry impellers. One of the main differences among the three impellers is the pitch ratio ranging from low to high, i.e. 0.44, 0.9 and 1.5 at the blade tip for the Maxflo Mark II, A312 and A100 impellers, respectively. The distance from the bottom wall was kept constant at 7.4 cm throughout the experiments. The flow field was evaluated at four different impeller clearances from the side wall (*E/D* = 0.26, 0.56, 0.62 and 0.72). This range covers *E/D* ratios used in other studies (Yackel, 1990; Bhole et al., 2011).

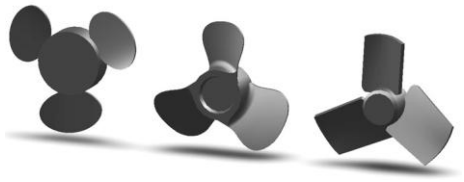

(a) (b) (c)

Figure 2-3. Axial flow impellers (a) Maxflo Mark II impeller, (b) A100 impeller, (c) A312 impeller

2.2 PIV settings[5]

The hub of the PIV system is inter-connected to the stirred tank by a triggering system that allows taking photos at specific impeller positions. At the moment the PIV hub receives the signal from the trigger, two consecutive light pulses are emitted by the laser.

The time between pulses, Δt, has to be set based on local velocities. As presented in Gomez et al., (2010), an optimum Δt is the time a particle (traveling perpendicular to the light sheet) would need to travel 25% of the light sheet thickness. It has been shown that the maximum velocity at only two millimeters away from the impeller can only be a fraction of the U_{tip} (30-50%) (Zalc et al., 2001; Bugay et al., 2002; Gomez et al., 2010), thus Equation 2-1 was used to determine Δt for each operating condition.

[5] Part of this section has been submitted for publication. **Sossa-Echeverria J. and Taghipour F., 2012. Mixing of Newtonian and Non-Newtonian fluids in a cylindrical mixer equipped with a side-entry impeller.**

$$\Delta t = \frac{0.8 Z_l}{U_{tip}} \qquad 2\text{-}1$$

The camera is synchronized to capture photos at the same time the laser emits light. Thus, two frames are acquired each time the impeller passes the trigger. These frames are processed in a computer using the software Flowmanager (from Dantec Dynamics) to obtain the velocity fields. Before processing the images, a grid has to be applied to each pair of photos. Two different grids (which define the velocity field resolution) i.e. 55×42 and 111×85 were used to create the velocity fields. The area of each element of the grid (known as interrogation window) was 4×4 mm^2 and 3.85×3.85 mm^2, respectively. The sizes of these frames are similar to those used by Torre et al., (2007), Couerbe et al., (2008) and Gomez et al., (2010), where characteristic flow structures were revealed for systems similar to the one used in this study. Each pair of images was processed using an adaptive correlation, which is based on cross-correlation techniques (Keane and Adrian, 1992). This technique reduces the size of the interrogation window progressively to improve the dynamic range and increase the space resolution (Scarano and Riethmuller, 1999). For this study, a single refinement step was used and an overlap of 25% between interrogation areas was included in the correlation process.

Steady-state flow fields at different conditions were obtained by averaging results of 800 instantaneous velocity fields. This number of measurements was found to represent the steady-state flow, since its comparison with a set of 1800 shows no significant change in the velocity vectors. The procedure to determine the appropriate number of photos is presented by Gomez et al., (2010).

2.3 Fluid rheology[6]

A basic requirement for a PIV system is an optically transparent work fluid. Therefore, a 99 w/w % glycerine solution with viscosity η = 1.1 Pa·s was used as model fluid for the viscous Newtonian fluid in this study. A similar solution was used by Gomez et al., (2010) to study the flow in a rectangular tank. On the other hand, aqueous carbopol solutions were used to represent complex rheologies of non-Newtonian fluids. Different carbopol concentrations yield different values for rheological properties like yield stress and pseudoplasticity. So, three aqueous carbopol solutions, 0.075, 0.09 and 0.1 w/w % were prepared using carbopol 940 (Noveon Inc.).

[6] Part of this section has been submitted for publication. **Sossa-Echeverria J. and Taghipour F., 2012. Mixing of Newtonian and Non-Newtonian fluids in a cylindrical mixer equipped with a side-entry impeller.**

At higher concentrations, the fluid displays significant viscoelastic effects, and at lower concentrations, the yield stress becomes insignificant. The polymer was completely hydrated with deionized water in a mixing tank. Then, the solution was neutralized to pH ≈ 7 using dilute NaOH (18 w/w %), and let stand for 24 hours. A detailed description of the preparation process is presented by Gomez et al., (2010b).

The characterization of the carbopol solutions was made using a DV-III Ultra Rheometer from Brookfield using vane and wide-gap cup geometry. Before measuring the yield stress, the material was pre-sheared at 0.5 rpm for 100 s, followed by a rest period of 100 s. The yield stress value was computed from the maximum torque measured as the motor rotated at 0.02 rpm. The effect of the angular speed on the measured torque was found to be less than 5% of the final yield stress. The time between torque readings was 5 seconds. Figure 2-4 shows the torque increments over time for four tests of a 0.075 w/w% carbopol solution. The maximum values correspond to the yield stress.

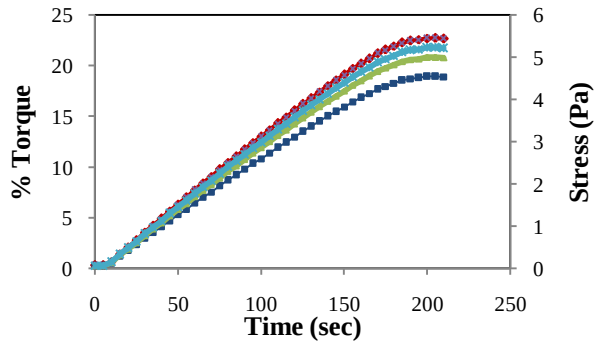

Figure 2-4. Yield stress measurements of a 0.075 w/w% carbopol solution. The yield stress value is 4.9±0.4 Pa (95% confidence interval)

The flow curves were obtained using the DV-III Ultra Rheometer in velocity control mode. For the vane and wide-gap cup geometry, Equations 2-2 and 2-3 can be used to plot the flow curves from torque and angular velocity measurements. The vane and cup geometry is treated as concentric cylinders to derive the expression (Equation 2-2) for the shear stress (Barnes and Nguyen, 2001). Assuming an infinite cup, Equation 2-3 can be used to calculate the shear rate (Steffe 1996).

$$\tau = \frac{M}{2\pi {R_b}^2 L_b} \qquad 2\text{-}2$$

$$\dot{\gamma}_b = 2\Omega \frac{dln\,\Omega}{dln\tau_b} \qquad 2\text{-}3$$

The flow curve for a 0.075 w/w% obtained using this approach was validated with results acquired using parallel plates and vane and cup geometries in stress control mode, and cone and plate in velocity control mode. As shown in Figure 2-5a the shear stress values for all methods fall over the same curve, except for the case of the cone and plate method. The difference might be due to a slip condition at the cone wall as reported by Magnin and Piau (1990).

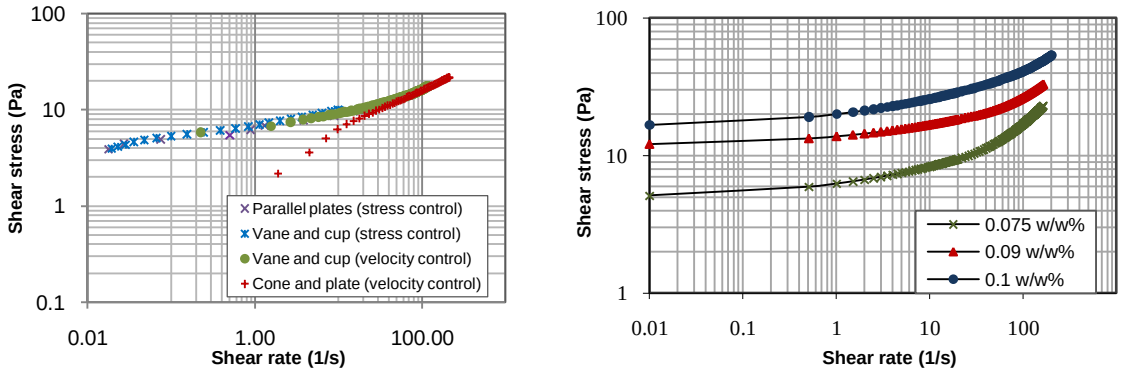

Figure 2-5. Flow curves of carbopol solutions (a) 0.075 w/w% using 4 different approaches. (b) Characterization of three carbopol concentrations.

The range of shear rates for the rheological measurements was selected based on the representative shear rate obtained from the Metzner and Otto expression ($\dot{\gamma} = K_s N$). An average shear rate of $\dot{\gamma} = 125\ s^{-1}$ was obtained with $K_s = 11$ (Chhabra and Richardson, 2008) and N= 11.4 s^{-1} (maximum rotational speed used throughout the experiments). The aim of this study was to cover the widest range of operating conditions in the laminar and transitional flow regimes. Thus, the highest angular speed was selected to be close to the turbulent regime. On the other hand, the yield stress of the carbopol solutions dictates the minimum velocity required to create a meani ngful cavern volume.

The Flow curves for the three carbopol concentrations are presented in Figure 2-5b. The shear thinning behaviour exhibited in the experimental results can be fitted using the Hershel-Bulkley model (Equation 2-4).

$$\tau = \tau_0 + k\dot{\gamma}^n \qquad 2\text{-}4$$

The parameters for the three solutions are presented in table 2-1. At high shear rates (above ≈ 30 s^{-1}) the viscosity of the carbopol solutions remains nearly constant at values of $\eta = 0.09$, 0.1 and 0.12 Pa.s, for the 0.075, 0.09 and 0.1 w/w% solutions, respectively.

Table 2-1. Parameters for the Hershel-Bulkley model

(w/w%)	τ_0 (Pa)	k (Pa.s^n)	n
0.075	4.9±0.4	1.32	0.4
0.09	10.8±0.8	1.99	0.4
0.1	16±0.9	3.94	0.4

3. Mixing behavior of Newtonian and Non-Newtonian fluids in a stirred tank equipped with a side-entry impeller[7]

The mixing behavior of a viscous Newtonian fluid (glycerine) and three non-Newtonian shear-thinning fluids with yield stress (carbopol solutions) is examined in this chapter based on flow visualization experiments. A cylindrical vessel equipped with an A100 impeller (rotating counter-clockwise) was used to carry out the experiments. The impeller clearance from the rear-wall was 7.5 cm.

3.1 Newtonian fluid

The bulk flow pattern of the glycerine solution at Re=35 is presented in Figure 3-1. Velocity vectors are colored by velocity magnitude (m/s). The velocity field at *Z*=0 (Figure 3-1a) pictures a radial flow pattern. The flow being dispatched from the impeller in the radial direction (represented by red vectors), and the circulation loops in front of and behind the impeller are typical characteristics of radial flow pattern. The unexpected radial flow (from this axial flow impeller) is due to the high viscosity of the fluid.

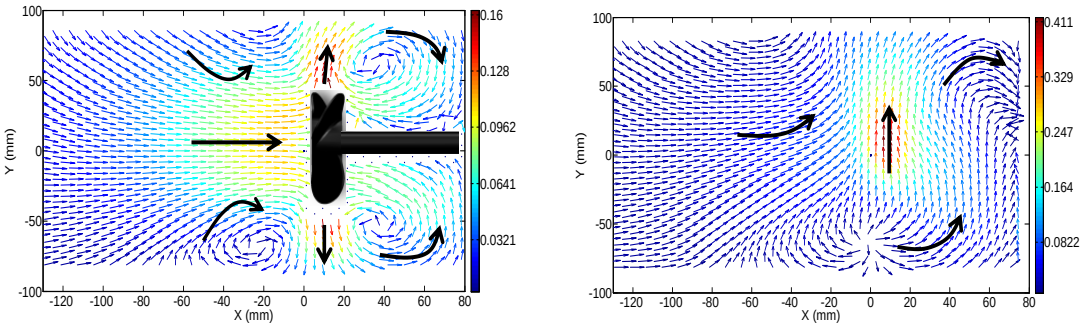

(a) (b)

Figure 3-1. Flow fields at Re=35, (a) *Z*=0, (b) *Z*=5. Velocity vectors colored by velocity magnitude (m/s). The wall behind the impeller is located at X=80 mm.

The lack of symmetry of the circulation loops in Figure 3-1a shows the strong effect of the vessel walls on the flow pattern. The loop in the bottom-right corner is confined by the bottom of the tank and the wall behind the impeller. Thus, the position and structure of this ring is nearly independent of the rotational speed. Likewise, the other two loops (top-right and bottom-left

[7] A version of this chapter has been submitted for publication. **Sossa-Echeverria J. and Taghipour F., 2012. Mixing of Newtonian and Non-Newtonian fluids in a cylindrical mixer equipped with a side-entry impeller.**

corners) are restricted in some extent by the tank walls. On the other hand, the loop in the upper-left side can move freely upward as the angular speed increases.

The effect of the high viscosity is reflected on the vector field at the plane close to the impeller tip (Figure 3-1b). The momentum transfer by diffusion is restricted in such a way, that at 3 mm away from the impeller tip, the highest velocity is only 50% of the tip velocity, U_{tip}. By comparing the maximum velocities at the two planes (Z=0 and Z=5), it can be stated that the tangential flow observed in Z=5 (Figure 3-1b) is stronger than the radial discharge detected at Z=0. This suggests that the high viscous forces are able to drag the fluid around the impeller in concentric and stable layers without significant changes in flow direction, which limit the exchange of material between layers.

The resistance to flow is also reflected in the steep decrease of the velocity in the axial direction (Figure 3-2). Figure 3-2a shows the normalized velocity profile of the suction stream at the center of the impeller. As expected, the highest velocity is found close to the impeller and it drops to almost zero in the axial direction in a distance equals to 1.5D. Likewise, at Z=5 (Figure 3-2b) the maximum velocity rapidly falls to zero in the "x" direction. The asymmetric distribution in Figure 3-2b reveals again the effect of the rear wall on the flow.

The velocity profiles in Figure 3-2 show that high velocity gradients only exist very close to the impeller (X*<2D). Therefore, there is a limited deformation of neighbouring layers in a considerable region of the tank, which restricts the mixing performance.

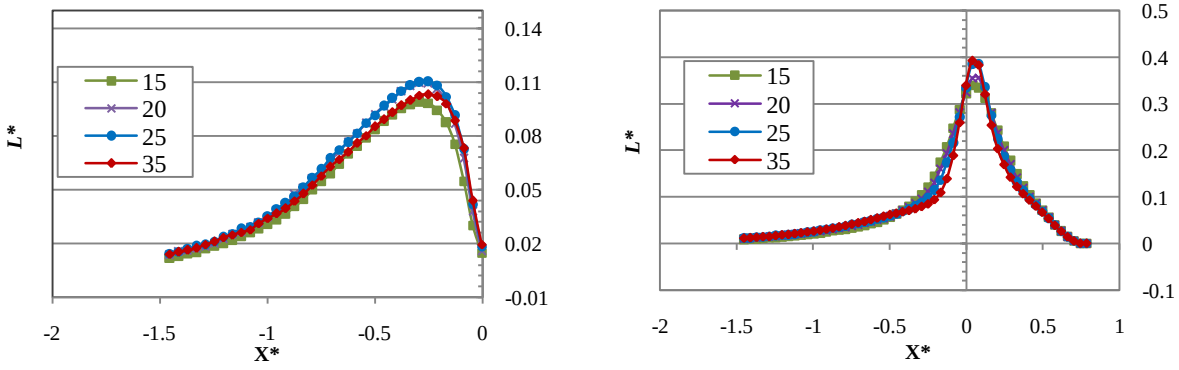

Figure 3-2. Normalized velocity (*L) vs. normalized axial distance (X*) over a sample line located at Y*=0 on the plane (a) Z=0 and (b) *Z*=5 for different Reynolds numbers**

In Figure 3-2, the horizontal profiles of normalized velocity at different rotational speeds tend to fall over the same curve. That is, at some locations of the mixing domain and over a certain angular velocity, the direction of the flow is independent of the Reynolds number. This is confirmed by the velocity fields plotted in Figure 3-3. The blue vectors correspond to Re=15 and red vectors to Re=35. Although, the magnitude of the vectors is different, the flow patterns at some locations are very alike for the two cases, e.g. the structure and position of the circulation loops below the impeller shaft.

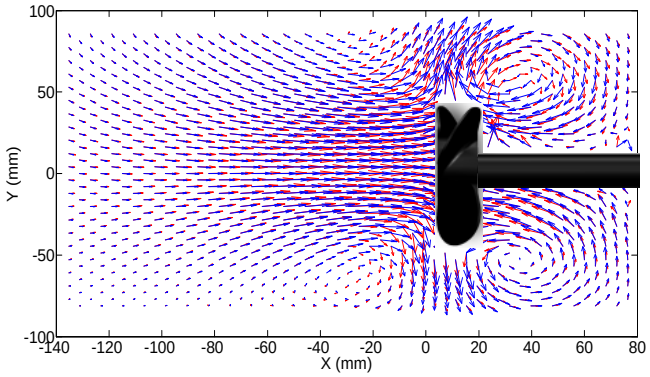

Figure 3-3. Velocity fields at *Z*=0. Blue vectors correspond to Re = 15 and red vectors to Re = 35. The tank wall behind the impeller is located at X=80 mm.

A quantitative comparison of the velocity profile under different Reynolds numbers is shown in Figure 3-4. The profiles correspond to the velocities over a line placed 30 mm behind the impeller at two different planes (*Z*=0 and *Z*=5). At both planes the profiles below the shaft overlap, which means that the bulk flow path remains the same regardless of the rotational speed. At *Z*=0 (Figure 3-4a) all the curves below the shaft go to zero at the same vertical distance, which confirms that the circulation loops are in the same location. In contrast, the profiles in the upper part portray different flow orientations at specific locations. This verifies the statement presented before, that the flow pattern in the lower part is driven by the walls of the tank (mainly the bottom and the wall behind the impeller). For the upper part, however, as the inertial forces increase the circulation loops are shifted upward, thereby breaking the symmetry of the pattern in the axial and radial directions.

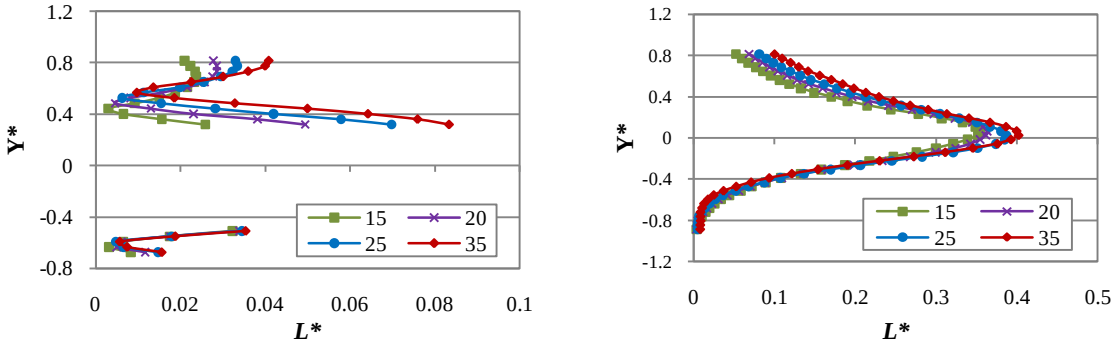

Figure 3-4. Normalized velocity (*L) vs. Normalized radial distance (Y*) over a sample line at X*= -0.31 on the plane (a) *Z*=0 and (b) *Z*=5 at different Reynolds numbers. In figure (a) the profile is not continuous because the impeller blocks the light coming from the laser before reaching that location, making the flow visualization impossible in those areas**

As previously discussed in this section, the high viscosity of the fluid prevents the axial discharge expected from the impeller utilized in these experiments. Moreover, the predominant tangential flow can severely affect the mixing quality, since part of the flow follows concentric and closed streamlines around the impeller without significant time-dependency. Likewise, the bulk flow is considerably affected by the spatial distribution of tank walls with respect to the impeller. The clearance to the bottom and rear-wall define the extent and position of some of the characteristic circulation loops of radial flow.

3.2 Non-Newtonian fluids

The bulk flow patterns at *Z*=0 and *Z*=5 are presented in Figure 3-5 for the 0.075 w/w% carbopol solution at 565 rpm. In this figure, the vectors in warm colors disclose the discharge of the impeller blades and the ones in cool colors show the streams going to the suction areas of the impeller. In Figure 3-5a, the mean axial-radial flow can be described as two jets discharged by the impeller blades, and two re-circulation loops that drive the flow towards the suctions regions (one behind the impeller and the other one at the center of the front face of the impeller). At *Z*=5 (Figure 3-5b), the region with high velocity vectors belongs to the discharge flow, and blue vectors show the path to the low pressure zone behind the impeller blade.

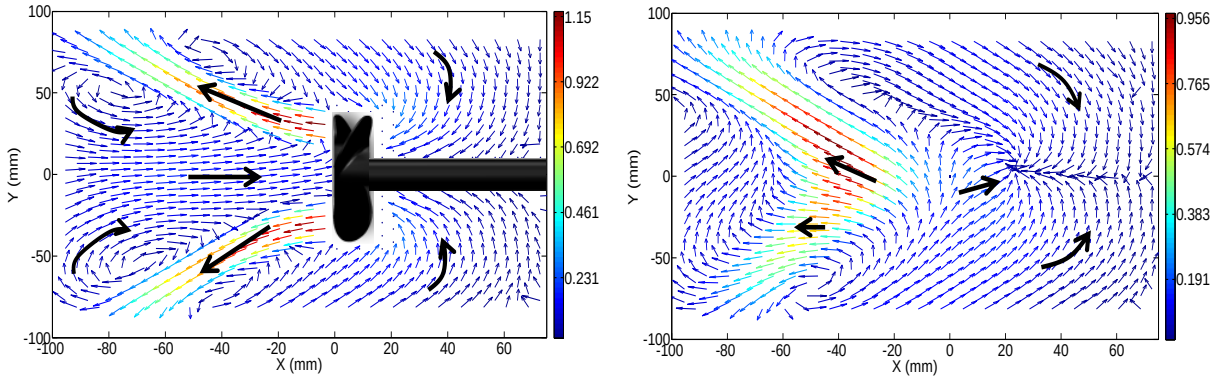

(a) (b)

Figure 3-5. Velocity fields of 0.075 w/w% carbopol solution at 565 rpm. (a) *Z*=0. (b) *Z*=5. Velocity vectors colored by magnitude (m/s). The tank wall behind the impeller is located at X=80 mm.

A geometrical idea of the three dimensional flow can be obtained by rotating the upper jet in Figure 3-5a 360^0 with the shaft as the rotating axis (blue structure in Figure 3-6). The created cone-shape structure represents the discharge region, and separates the re-circulation streams that return the fluid to the impeller (red and green structures in Figure 3-6). The outer region of the cone is identified as the main circulation loop, since most of the fluid returns to the low pressure zone created behind the impeller. The entrainment caused by the opposite flow of the strong impeller discharge and the suction streams, creates small circulation loops in the vicinity of the jets. The material exchange between these circulation loops and the bulk flow is very limited, which resembles segregated structures found in other studies (Arratia et al., 2006).

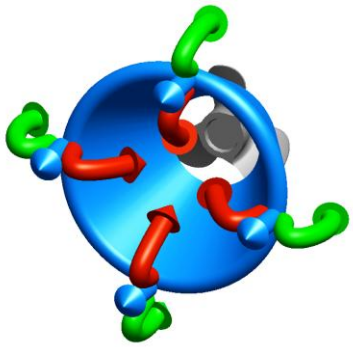

Figure 3-6. Three dimensional description of the flow. The blue structure represents the impeller discharge, and the red and green arrows symbolize the fluid returning to the suction zones at the center of the impeller and behind the blades, respectively.

Unlike the flow pattern generated with the Newtonian fluid, the highest velocity is on the plane *Z*=0. This confirms the weakness of the tangential flow in the case of the non-Newtonian fluid.

The strong axial flow is also represented by large x-components of the velocity at both planes (Figure 3-5a and 3-5b), particularly close to the impeller blades. This implies that inertial forces are dominating the flow, especially near the blades where low viscosities are likely due to the high shear rates.

The flow characteristics previously described are affected by the rheological properties of the fluid and the operating conditions. A comparison of the velocity fields for the highest and lowest concentrations is presented in Figure 3-7. The blue vectors describe the flow of the 0.1 w/w % solution and the green ones for the dilute solution of 0.075 w/w %. The effect of the yield stress is reflected in the extent of the cavern. The higher yield stress of the concentrated solution (τ_y ≈16 Pa) restrains the dynamic zone in a smaller volume compared to the more dilute solution with $\tau_y \approx 5\ Pa$. In the vertical direction, the boundaries of both caverns are outside of the velocity field. However, in the horizontal direction it is clear that the limit of the concentrated solution is less than half of the dilute solution.

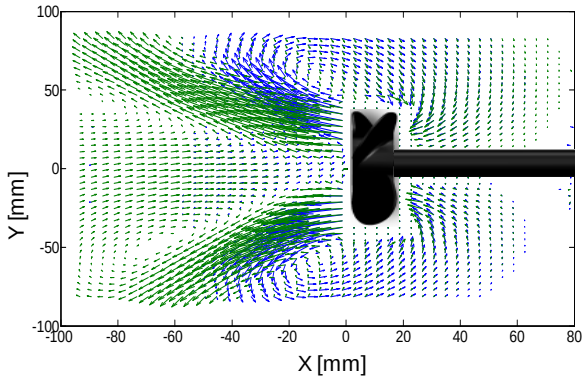

Figure 3-7. Velocity fields at *Z*=0 for 0.075 w/w% (green vectors) and 0.1 w/w% (blue vectors) carbopol solutions. The tank wall behind the impeller is located at X=80 mm.

Another notable difference between the flow patterns is the discharge angle, defined as the angle of the jets with respect to the axis. The discharge angles of the upper jets at X*=0.3 were found to be 26^o, 29^o and 32^o for the 0.075, 0.09 and 0.1 w/w % respectively. The discharge angle is not axisymmetric, since the bottom wall of the tank limits the growth of the cavern downwards. This limitation becomes significant when the cavern is big enough to interact with the wall. Thus, for the highest concentration the effect is almost negligible as seen in Figure 3-7, where the flow is nearly symmetric. However, for the lowest concentration, the extent of the jet below the impeller is smaller compared to its counterpart above the impeller. The dependency of the discharge

angle and the carbopol concentration can be related to the flow consistency index. Thus, the lower the consistency index, the smaller the discharge angle. At high consistency indexes the viscous forces become significant and the discharge flow develops an important radial component, as shown in the case of the viscous fluid in the previous section.

The effect of the high viscosity is also reflected in the maximum velocity at the discharge zone on the plane *Z*=0, which are 37, 34 and 32% of the U_{tip} for the 0.075, 0.09 and 0.1 w/w% solutions, respectively. Assuming a no-slip condition at the blade walls, the tangential component of the velocity is expected to be higher for the more concentrated solution. This directly affects the pumping capacity as shown in Figure 3-8, where the lowest pumping values are observed for the most concentrated solution. The pumping number was evaluated at 327, 416, 565 and 684 rpm for each carbopol solution. The Yield-stress Reynolds number (Equation 3-1) has been used in other studies to characterize impellers and mixing performance in fluids with yield stress (e.g., Pakzad et al., 2008, Bhole and Bennington, 2010). The use of the factor (3.6×10^{-7}) in equation 3-1 is to adjust the selected unit inputs.

$$Re_y = 3.6 \times 10^{-7} \frac{\rho N^2 D^2}{\tau_y} \qquad 3\text{-}1$$

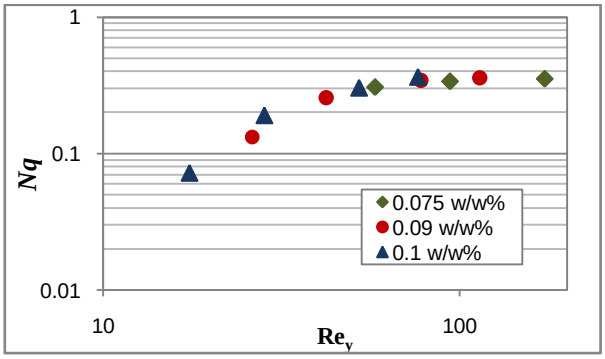

Figure 3-8. Characteristic pumping number (*Nq*) Vs. yield-stress Reynolds number (Re_y) curve for the A100 impeller.

The pumping number was calculated with the volumetric flow passing through a circular plane drawn by one revolution of the impeller and placed at X*= 0.07 (Jaworski et al., 1996). Since the flow at the given position is symmetric, the profile of the mean *U* velocity (x-component of the velocity) from the impeller center to the blade tip was applied to integrate the flow area. From

the pumping number curve, it can be stated that all the laboratory tests were performed between laminar and transitional flow regimes.

The cavern shape and the flow pattern in the active zone are determined by the discharge angle and the strength of the jets. As the discharge angle increases, the active zone adopts a toroidal shape around the impeller, and the small circulation loops created by entrainment tend to merge with the suction streams. When the axial flow is significant, the cavern develops more complex geometrical shapes, and secondary circulation loops arise. The normalized weighted average of the *U* velocity in Figure 3-9a, shows how the flow becomes more axial (larger x-component of the velocity) as the carbopol concentration increases. This trend is replicated on the three planes; hence, the axial flow condition can be extended to all the mixing volume. The increase of the axial component takes place without compromising the flow in the "y" direction. Figure 3-9b shows how the *V* velocity (y-component of the velocity) also raises over the entire volume as the concentration decreases. However, the incremental ratio is lower compared to the one of the *U* velocity. This confirms that the high weighted average of the *U* velocity for the lowest concentration is not only the result of a lower resistance to flow (due to the low viscosity), but also a re-arrangement of the flow structure, which tends more towards the axial direction.

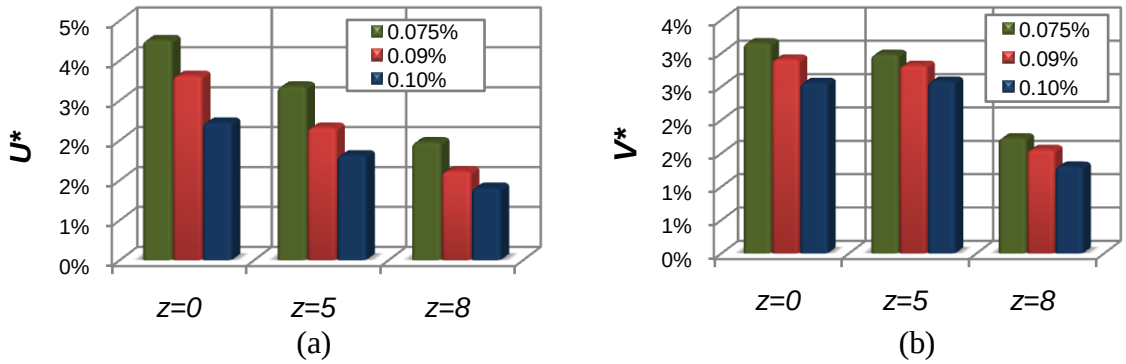

Figure 3-9. Normalized weighted average of (a) x-component of the velocity, (b) y-component of the velocity

Certainly, the impeller discharge is also affected by the rotational speed. Figure 3-10 shows the vector maps for the 0.075 w/w % solution under different angular speeds. As expected, the increase of inertial forces boosts the cavern size and the axial flow. The stronger jets shift the small circulation loops away from the impeller. Likewise, they make the fluid swirls in bigger areas and at higher rates due to the enhanced vortices created in the inner and outer sides of the

jets. The maximum velocities of the jets on the plane Z=0 are 28.8, 32.2, 36.0 and 37.6% of U_{tip} at 327, 416, 565 and 684 rpm, respectively. The increase of the planar velocity reflects a decrease in the tangential flow as presented previously.

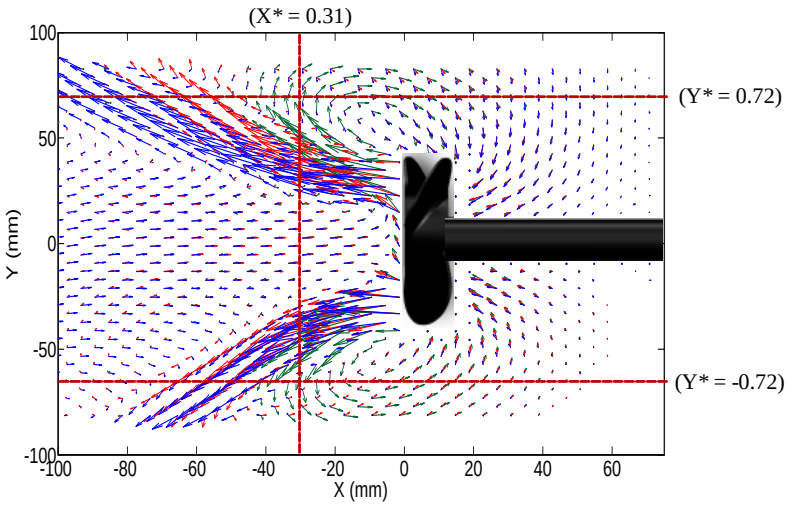

Figure 3-10. Velocity fields of 0.075 w/w% carbopol solution at 327 (green vectors), 565 (red vectors) and 684 rpm (blue vectors). The tank wall behind the impeller is located at X=80 mm.

It can be observed from Figure 3-10, that the discharge angle approaches a constant value as the angular speed increases. The velocity fields of subsequent velocities tend to overlap as the rotational speed increases. This behaviour is more notorious in the lower half of the vector map, and is confirmed by the normalized velocity profiles plotted in Figure 3-11. At Y*=-0.72 (Figure 3-11a) the profiles are very similar, especially at high velocities when the interaction between the cavern and the vessel wall is significant. As mentioned before, the bottom wall defines the flow structure in the lower region of the tank over certain flow discharge. On the other hand, at Y*=0.72 (Figure 3-11b) the profiles bare little, mainly because the flow in the upper part can change without physical restrictions. However, there is a clear trend of the peaks approaching a maximum L^* ($L^*=L/U_{tip}$). The peak values are the maximum velocities of the jets at the given Y*. This means that for some locations and under certain conditions the flow direction is independent of the rotational speed. Thus, the previously observed effect of the viscous forces on the flow structure becomes less noticeable. This behaviour is confirmed by the similarity of the velocity profiles over a vertical sample line close to the blades at Z=0 and X*=0.31 (Figure 3-11c). Two possible reasons of this behaviour are: 1) turbulent flow near the blades, which diminishes the effect of the viscous forces or 2) the Newtonian behaviour of the carbopol

solutions at high shear rates (near the blades) that makes the viscosity independent of the angular speed.

The bulk flow pattern observed for the three carbopol solutions differs significantly from the flow pattern of the viscous Newtonian fluid. The given low viscosity of the carbopol solutions next to the impeller blades allows the impeller to discharge with a stronger axial component. The yield stress delimits the boundary of the active zone, and the Reynolds number defines the shape and the flow structure inside this zone.

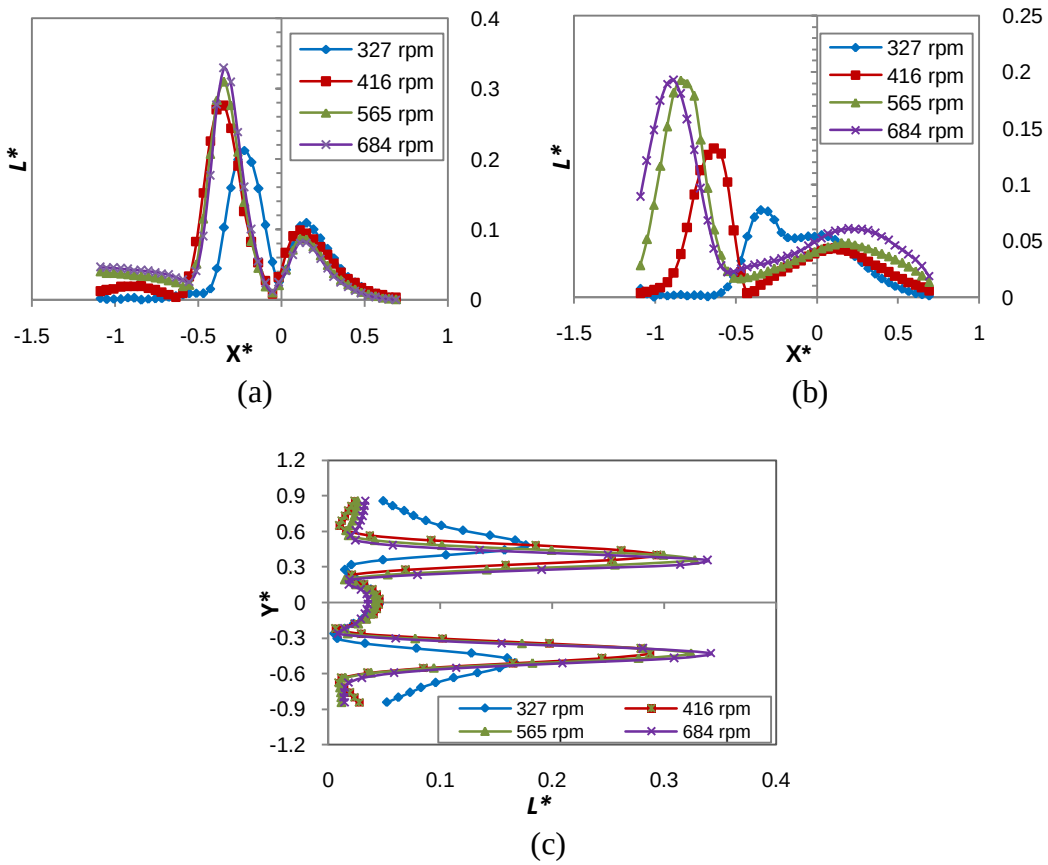

Figure 3-11. Normalized velocity profiles at (a) Y*= -0.72, (b) Y*= 0.72 and (c) X*=0.31. The positions of these sample lines are shown in figure 14.

4. Effect of mixer geometry and operating conditions on flow mixing of non-Newtonian fluids[8]

The following chapter discusses the effect of some geometrical parameters (mixer shape and impeller type and position) on the flow pattern, based on velocity fields obtained at different locations inside the mixing domain. The model fluid used for this study was the 0.09 w/w% carbopol solution.

4.1 Impeller clearance from vertical wall

The flow generated by an A100 impeller at 565 rpm is presented in Figure 4-1. The mean axial-radial circulation can be described as two strong jets coming out from the impeller blades. The flow is re-circulated through two main loops; in one loop flow goes towards the low pressure zone of the impeller while in the other one the flow moves towards the center of the front face of the impeller. In Figure 4-1, the strong segregation of the flow and the boundary of the active mixing zone are also evident.

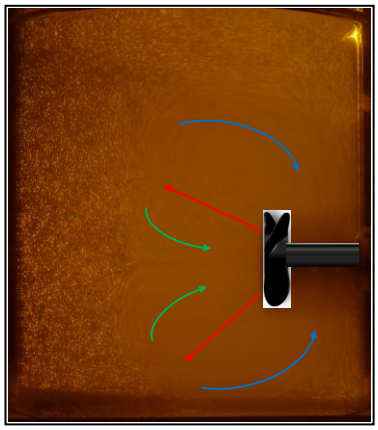

Figure 4-1. Flow visualization at Z=0, showing the strong jets coming out from the impeller blades (red), the circulating loop going towards the low pressure zone behind the impeller (blue) and the circulating flow towards the front center of the impeller (green).

The flow fields of the three evaluated clearances are presented in Figure 4-2. The main differences among the three cases are the discharge angle and the strength of the jets, which significantly affect the size and shape of the active mixing zone. The discharge angle was

[8] A version of this chapter has been submitted for publication. **Sossa-Echeverria J. and Taghipour F., 2012. Effect of mixer geometry and operating conditions on flow mixing of shear thinning fluids with yield stress.**

calculated by averaging the angle with respect to the impeller axis of all the vectors going from right to left at X*= 0.35 (Figure 2-2c). The discharge angles at *E/D*=0.26, 0.56 and 0.62, were determined to be 40^0, 32^0 and 30^0, respectively. The effect of clearance on the jet strength can be evaluated by examining the velocity at an axial distance away from the impeller. At X*=0.5 the maximum velocity for the shortest clearance (*E/D*=0.26) was 29.7% of U_{tip} (tip speed) whereas at *E/D*= 0.62 it was 36.7%.

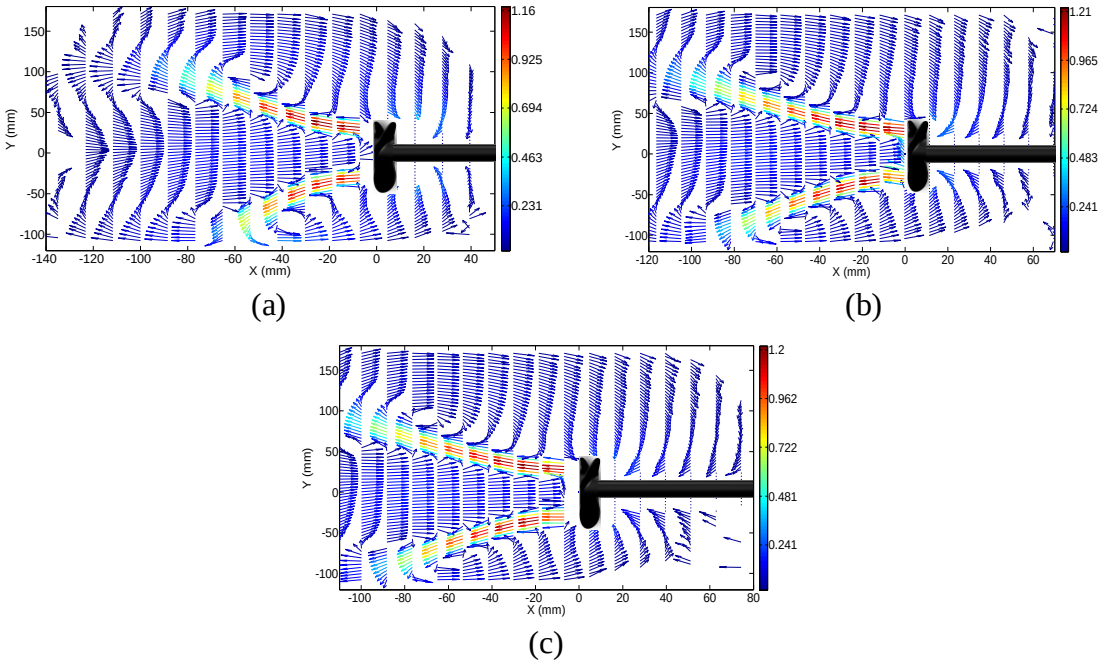

Figure 4-2. Mean planar velocity fields at *Z*=0 for (a) *E/D*=0.26, (b) *E/D*=0.56, (c) *E/D*=0.62. Velocity vectors colored by velocity magnitude (m/s)

The effect of clearance is only significant when there is a strong interaction between the active zone and the vessel walls. At 416 rpm the cavern does not reach the wall behind the impeller, and the effect of clearance is negligible. As shown in Figure 4-3a, there is a noticeable similarity among the velocity profiles across a vertical sample line (X*=0.07) for the 3 different clearances. On the other hand, at 684 rpm (Figure 4-3b) there are considerable differences, especially at the height of the impeller discharge (Y*≈ 0.3), where the velocity is higher for the two largest clearances. This suggests a positive correlation between clearance and cavern size, and is supported by the velocity distributions in Figure 4-4. Interdependency between clearance and cavern size has been found by others e.g., Yackel, (1990) and Bhole et al., (2011).

The probability density functions (PDF) of the velocity magnitude for two vector maps (Z=0 and Z=5) are shown in Figure 4-4. The PDF is a function that provides the probability of a random variable being within a specific interval when integrated over the same interval. The function is computed from the smallest to the largest values of the variable at the specific plane, using a normal distribution. The probability of values out of the plotted range is equal to zero.

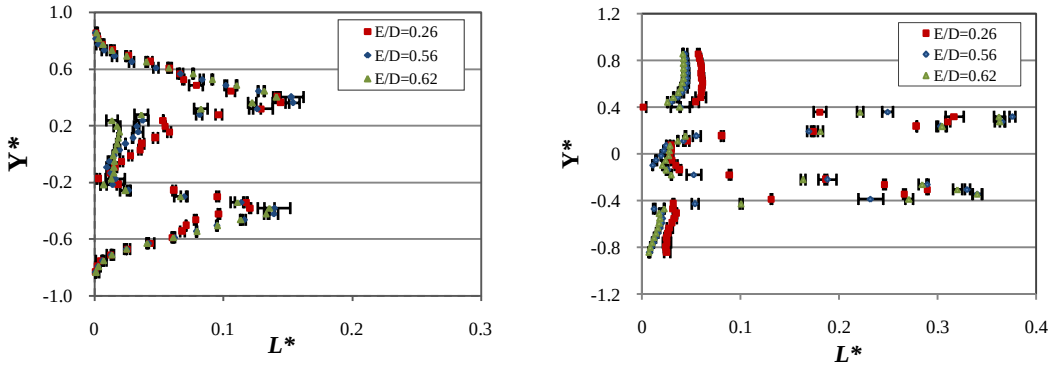

(a) (b)

Figure 4-3. Normalized velocity profiles L^* at X = 7.5 mm and plane Z=0 for (a) N=416 rpm. (b) N=684 rpm. The error bars indicate the standard deviation for three measurements.

At E/D = 0.26 an unfavourable condition arises, since the average velocity is lower compared to the other cases. Another observation is the uneven distribution of velocities for the 3 clearances, where significant probabilities exist for velocities below 10% of U_{tip}. The high velocity values at the tail of the distribution correspond to the small fraction of fluid leaving the impeller blades in the axial direction. The lower velocities represent most of the active area, where high viscosities predominate due to the low shear rates.

In general, it was found that the cavern volume and the average velocity near the impeller can be enhanced by increasing the clearance from the rear wall. However, this progress curve tends to a maximum, where high values (over 0.56 for the E/D ratio in this case) do not provide significant improvement.

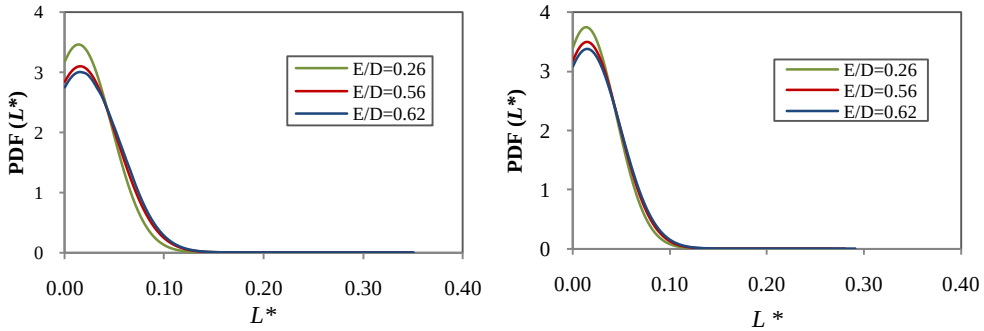

Figure 4-4. Probability density functions (PDF) of the normalized velocity (*L), at various clearances on (a) *Z*=0, (b) *Z*=5**

4.2 Vessel shape: cylindrical and rectangular

The cylindrical and rectangular vessels showed in Figure 2-2a and 2-2b were used to evaluate the effect of vessel shape on the macroscale structures of the flow. Since the shortest clearance accentuates the interaction between vessel walls and cavern, the *E/D* was set to 0.26 to study such effect. Figure 4-5 shows velocity fields at Z=0 for the two cases. For the sake of clearness only velocity vectors with magnitudes over 2% of U_{tip} were plotted, showing an approximate cavern size and shape for the two tanks. The flow structures are very similar, but the region occupied by the vectors corresponding to the rectangular vessels is noticeably larger, especially in the upper part.

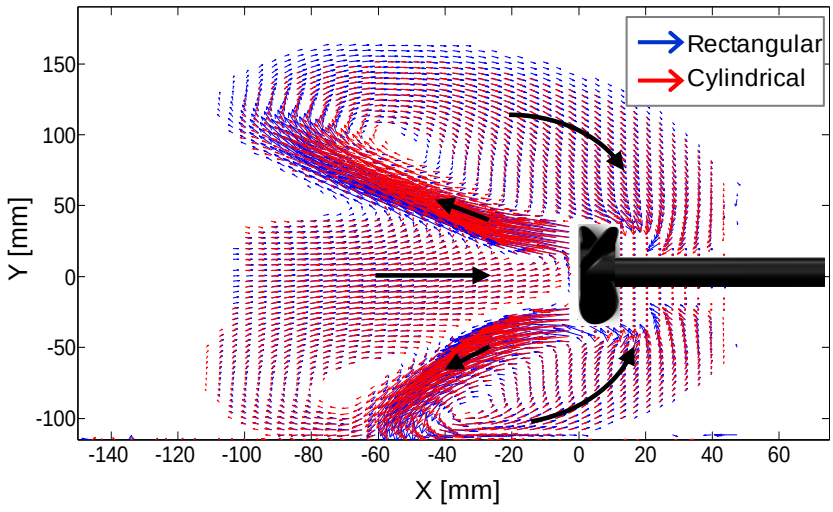

Figure 4-5. Mean planar velocity fields at 684 rpm for *Z*=0 in rectangular and cylindrical vessels

A quantitative comparison is presented in Figure 4-6 for two different impeller velocities. At 327 rpm (Figure 4-6a), the caverns do not touch the vessel wall, resulting in the overlapped velocity profiles. Contrariwise, at 684 rpm there are some locations within the cavern with major velocity differences. At the higher rpm the rectangular vessel offers a peak velocity 18% higher than the velocity of the cylindrical vessel at $Y^* \approx 0.3$ (velocity of the jet). Another observation shown in the upper part of the curves is that the extent of the motion is larger for the rectangular tank. This statement can be extended to the entire fluid domain, since at Z=5 similar differences can be observed. Thus, a larger cavern size is obtained when mixing takes place in the rectangular tank.

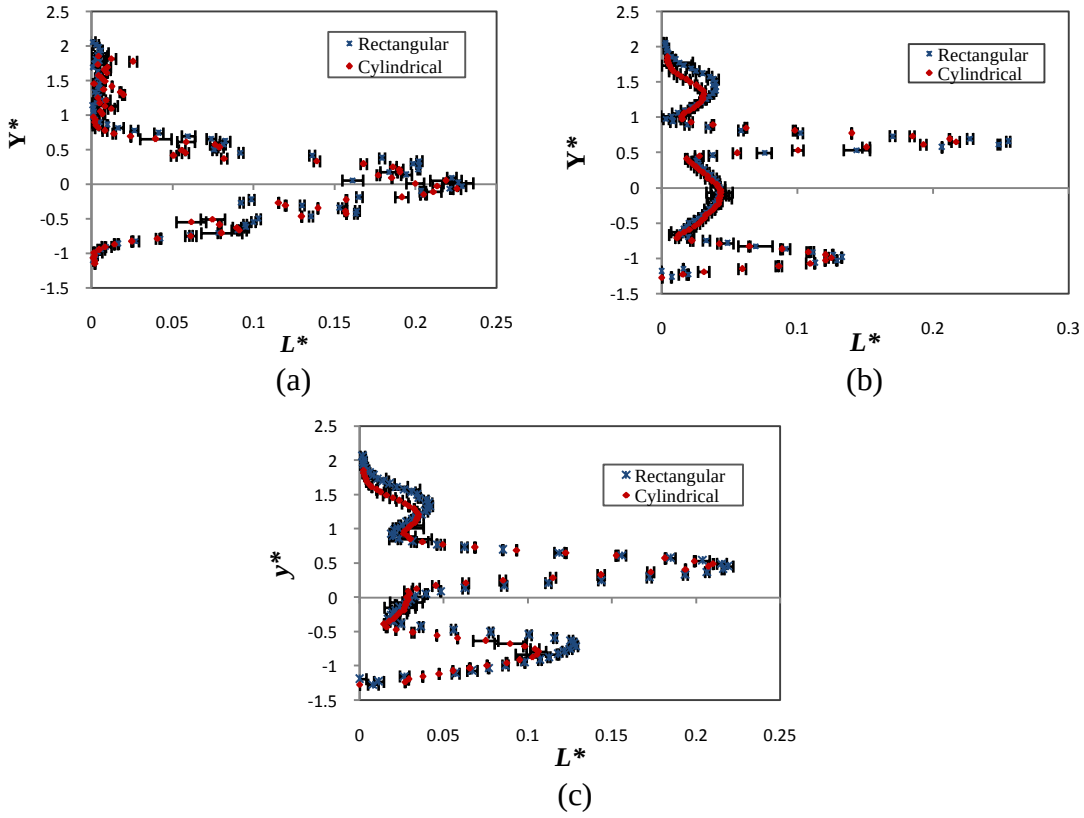

Figure 4-6. Velocity profiles at X=50 mm for (a) *Z*=0 and *N*=327 rpm, (b) *Z*=0 and *N*=684 rpm and (c) *Z*=5 and *N*=684 rpm

A noticeable characteristic of the velocity profiles at 684 rpm (Figure 4-6b and 4-6c), is an axi-asymmetric pattern having higher velocities for the upper jet. This reflects how the clearance from the bottom wall of the vessel can restrict the evolution of the flow and the extent of the dynamic zone.

The combined effect of clearance from the rear-wall and vessel shape was assessed by defining a margin velocity. Although this limit is not the actual boundary between the cavern and the dead

zone, it provides a baseline to compare the extent of the cavern under different suction areas. The boundary velocity was set following the approach presented in Adams and Barigou (2007), where 1% of the U_{tip} is assumed to indicate the limit of the pseudo-cavern. The distance from impeller center to this limiting boundary was measured in the plane Z=0. This was done for both axial and radial directions, under different combinations of clearance and vessel shape. The suction area was calculated as πDI, where D is the impeller diameter and I is the length from impeller tip to rear-wall. The results, presented in Figure 4-7, show a clear trend where the cavern volume increases with enlarging the suction area. At small suction areas, there is a considerable restriction of the flow to the suction zone behind the impeller. The restriction constrains the contribution of the inertial forces and consequently the extent of the cavern. To attain a certain flow pattern, this decrease of inertial forces may be compensated with higher rotational speeds, which will in turn increase the power consumption. The relationship between cavern size and suction area is not linear and tends to reach an asymptote that is related to the maximum pumping capacity of the impeller. Above 22000 mm^2 the cavern growth is not significant and the E/D ratio for this suction area ($E/D \approx 0.5$) agrees with optimum E/D ratios presented in literature for mixing of pulp suspensions with side entry impellers (Yackel, 1990; Reed, 1995; Bhole et al., 2011).

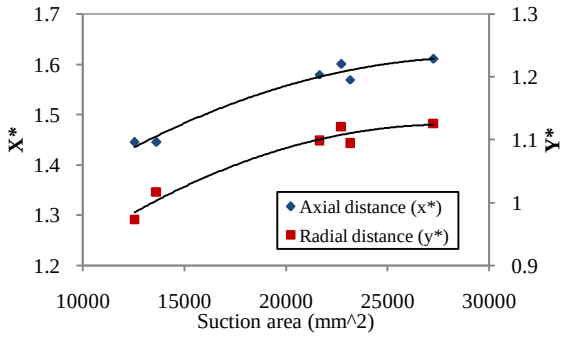

Figure 4-7. Cavern extent vs. Suction area

4.3 Impeller geometry

Measurements were carried out for three axial flow impellers with different blade angles. The Yield-stress Reynolds number (Equation 3-1) was used to characterize the impeller performance. The velocity distributions for each impeller are presented in Figure 4-8. The N_p vs. Re_y and N_q vs. Re_y curves are presented in Figure 4-12.

The flow-structures generated by the three impellers (at 684 rpm) show significant differences. The effect of the pitch ratio (0.44, 0.9 and 1.5 for the Maxflo, A312 and A100, respectively) is reflected on the discharge angle and jet size and shape, which define the characteristics of the cavern. Thus for the Maxflo, a weak jet with a high discharge angle with respect to the axis produces a small cavern with a toroidal shape around the impeller. Characteristics of the A312 and A100 flow include bigger cavern size and smaller discharge angles, which allow the cavern to grow in the axial direction. This flow pattern generates a kidney-like shape cavern and induces a reversed flow towards the center of the front face of the impeller.

The location of the highest velocity at Z=0 is for all cases Y ≈ 30 mm and X ≈ 5 mm. However, the magnitudes differ considerably between one another. The velocities are 15%, 23% and 35% of the U_{tip} for the Maxflo, A312 and A100, respectively. Similar low velocity conditions have been reported in other studies (Kumaresan and Joshi, 2006; Gomez et al., 2010).

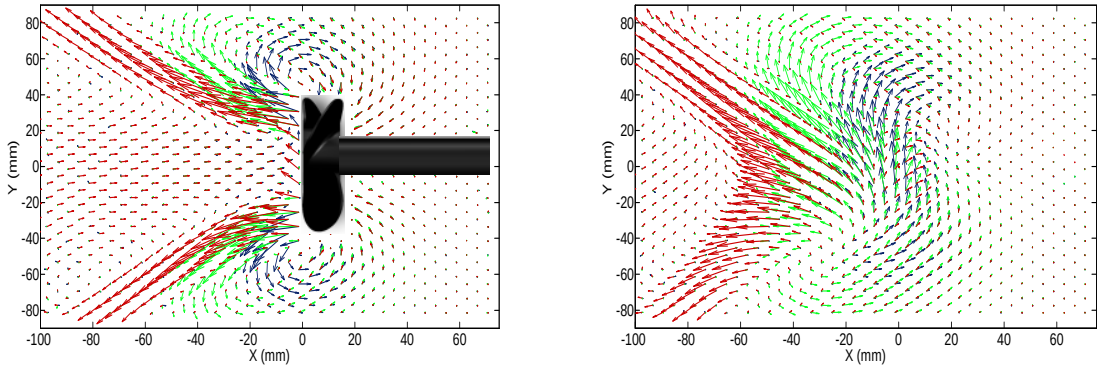

(a) (b)

Figure 4-8. Average velocity fields at 684 rpm for three different impellers. Blue vectors correspond to the Maxflo Mark II, green vectors correspond to the A312 and red vectors correspond to the A100 at (a) *Z*=0 and (b) *Z*=5

The differences in the three flow patterns are reflected not only at Z=0, but also at Z=5 (Figure 4-8b), where higher velocities and stronger axial discharge are observed for the A100. At Z=5, the strong tangential flow for the Maxflo, implies that part of the fluid is being dragged around the impeller in concentric lines as it rotates. On the other hand, the axial components of the velocity for the A312 and particularly for the A100 become more significant in the velocity map. These differences are related to the angle of attack of each impeller, which is described by the pitch ratio. The highest pitch ratio of the A100 impeller implies the highest angle of attack. This characteristic allows the blade to disrupt the closed streamlines produced by the viscous forces

and imparts momentum in the axial direction more effectively. Additionally, lower viscous forces are expected in the discharge zone of the A100, since the shear rate in the vicinity of this impeller is higher compared to the Maxflo and A312 impellers (Kumaresan and Joshi, 2006).

Figure 4-9 shows the velocity vectors with magnitudes above 1×10^{-3} and below 0.14 m/s to better show the flow characteristics. In Figure 4-9a the strong discharge of the A100 produces regions with large vorticity and perhaps higher shear rates due to the high velocity gradients in the vicinity of the jets (located on the white spaces). Moreover the interaction between the discharge flow and the streams going back to the suction areas in front of and behind the impeller, create small circulations loops at the inner and outer side of the jet.

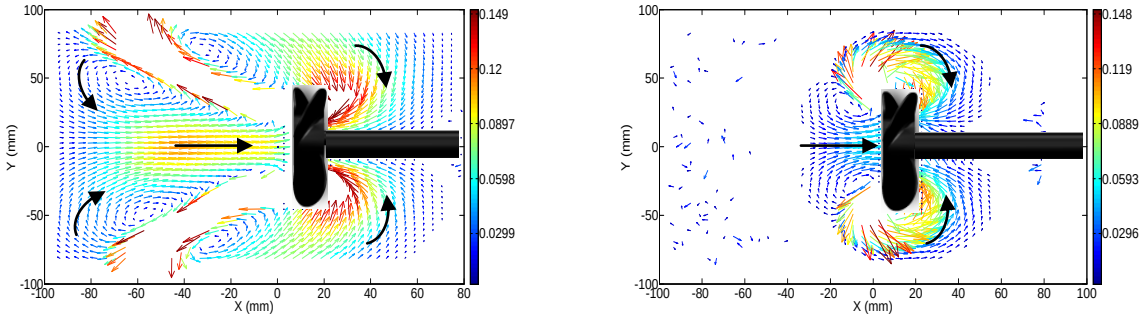

(a) (b)

Figure 4-9. Mean planar velocity fields at 565 rpm in *Z*=0 for (a) A100 impeller and (b) Maxflo Mark II impeller. Velocity vectors colored by velocity magnitude (m/s)

It is believed that those circulation loops are segregated zones from the bulk flow, since high concentrations of dye are observed at those positions without significant change over time (Figure 4-10). As the discharge angle decreases (higher angular speed), the small circulation loops move away from the impeller in the axial and radial direction and the reversed volumetric flow coming through the center becomes prominent. For the Maxlfo (Figure 4-9b), the quasi-radial discharge drives most of the fluid to the low pressure zone of the impeller through one main circulation loop. Due to the short extent of the jets, the additional circulation loop at the outer side of the jet observed for the A100 merges with the suction stream behind the impeller. In this figure the small-toroidal active zone is evident for the Maxflo, while the cavern limit for the A100 impeller is outside of the area covered by the PIV photos.

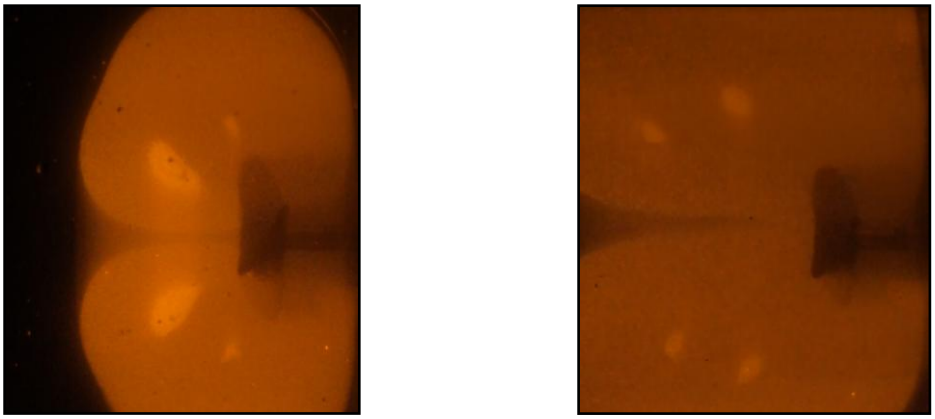

(a) (b)

Figure 4-10. Photography of segregated circulation loops at (a) 327 rpm, (b) 416 rpm

A quantitative comparison of the axial-radial flow generated by the three impellers is exposed in Figure 4-11. The figure shows the probability density function (PDF) of the velocity magnitudes in the "x" and "y" directions on the plane Z=0 for each impeller. The predominant axial flow for the A100 is reflected by the wider distribution of U^* and the lower probability of velocities close to zero (Figure 4-11a). Figure 4-11b shows that the increase in axial flow occurs without losing the radial component of the velocity; hence the cavern grows in both directions.

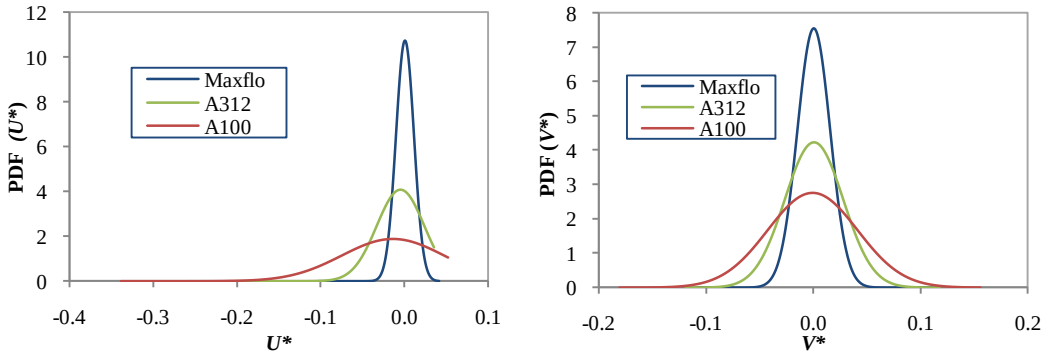

(a) (b)

Figure 4-11. Probability density function on the plane Z=0 of (a) Normalized x-component of velocity. (b) Normalized y-component of velocity

The pumping number vs. Yield-stress Reynolds number curve (Figure 4-12b) confirms the laminar-transitional flow regime and the prevailing axial discharge of the A100 impeller. The pumping capacity was defined as the volumetric flow rate passing through a circular plane with

the same radius and center as the impeller, placed 7 mm in front of the impeller. Based on the velocity symmetry shown in Figure 4-8a, the velocity profile (from Y*=0 to Y*=0.5) of the mean velocity normal to the surface was used to integrate the flow area (Jaworski et al., 1996

Overall the results indicate that a higher pitch ratio provides bigger cavern size and improves mixing performance when axial flow is desired. Although the power requirements for the low pitch ratio are lower, the required mixing mechanisms in the laminar regime can be negatively affected by the lack of perturbation of the streamlines created by the viscous forces.

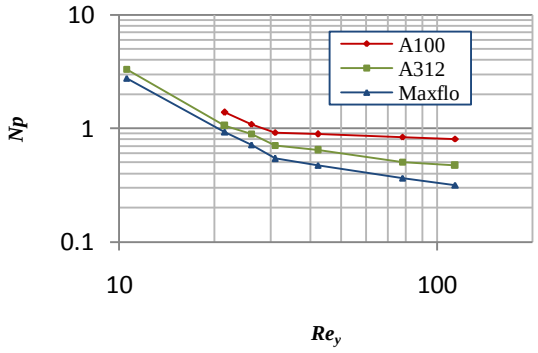

(a)

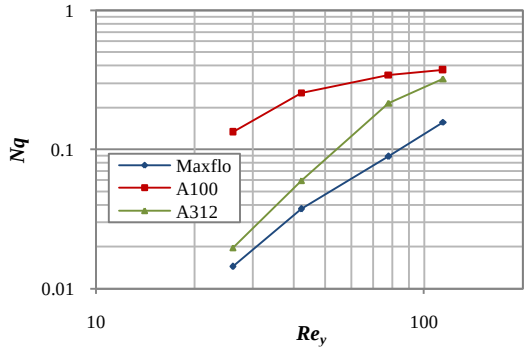

(b)

Figure 4-12. (a) Pumping number vs yield stress Reynolds number and (b) Power number vs. yield stress Reynolds number

5. CFD study of mixing flow of Non-Newtonian fluids in a stirred tank equipped with a side-entry impeller[9]

Computational fluid dynamic (CFD) models of the cylindrical tank equipped with three different impellers (Figure 5-1) were built to obtain information on segregated zones, three dimensional flow structures, shear rate distributions, and cavern size and shape under different mixing conditions. The clearance from the rear wall (*E*) in this study was kept constant at 7.5 cm (optimum *E* value as shown in chapter 4).

(a) (b) (c)

Figure 5-1. Top view of axial flow impellers. (a) A100, pitch ratio=1.5, (b) A312, pitch ratio=0.9, (c) Maxflo Mark II, pitch ratio=0.44.

5.1 Model development

The fluid dynamics inside the mixer was determined by solving the governing equations of mass and momentum conservation in steady-state for an incompressible fluid using ANSYS Fluent (CFD software). The flow domain was divided into three cylinders for the meshing process: 1) A cylinder enclosing the impeller. 2) A hollow cylinder for the bottom half of the tank enclosing the cylinder mentioned before. 3) A cylinder for the top half of the tank (Appendix A). Three CFD models were created; one for each impeller. The models reflect the actual tank and impeller geometries. The impeller shaft and the small mounting supports of the impellers were not considered in the geometries. During the meshing process, an advanced size function was used around the impellers to accurately capture the blade geometries. The final computational meshes range from 1,033,222 to 1,481,631 elements.

Grid independence was checked by comparing converged results of set of grids with a global refinement factor close to 1.3. The refinement process was done by keeping the size function and reducing the size of the elements next to the impeller surface. Velocity profiles close to the impeller and the torque on the impeller were compared for two consecutive grid resolutions. If

[9] A version of this chapter has been submitted for publication. **Sossa-Echeverria J. and Taghipour F., 2012. CFD study of mixing flow of non-Newtonian fluids in a stirred tank equipped with a side-entry impeller.**

the differences were below 5%, the grid with the less number of volumes was considered grid-independent and was used for further evaluations during the study (Appendix B). The requirements for a converged solution were: second order upwind scheme for the convection terms, normalized residuals for velocity and pressure below 1×10^{-5} and relatively steady velocity values during 1000 iterations.

The impeller rotation was modeled using the Moving Reference Frame (MRF) method available in Fluent. In this study the impeller was placed in a manner that one of the blades was vertically align with the shaft and pointing towards the bottom wall of the tank. The flow in the cylinder enclosing the impeller was calculated by solving the equations in a moving reference frame, and the remainder of the vessel in a stationary reference frame. No-slip condition was used at all solid-liquid boundaries and zero flux of all quantities was set across the fluid surface. The observed lack of motion over the fluid surface during the experiments supports the last boundary condition.

Each of the flow curves obtained from rheological measurements of the three carbopol solutions (0.075, 0.09, 0.1 w/w%) can be described by three different expressions (Figure 5-2a). The resistance to flow at stresses below the yield stress can be approximated by assuming a very viscous fluid at very low shear rates. As the shear rate increases and the yield stress is overcome ($\dot{\gamma} > \dot{\gamma}_0$), the fluid displays pseudoplastic behaviour until it reaches a given shear rate $\dot{\gamma}_b$, where the viscosity remains constant regardless the shear rate (Figure 5-2b).

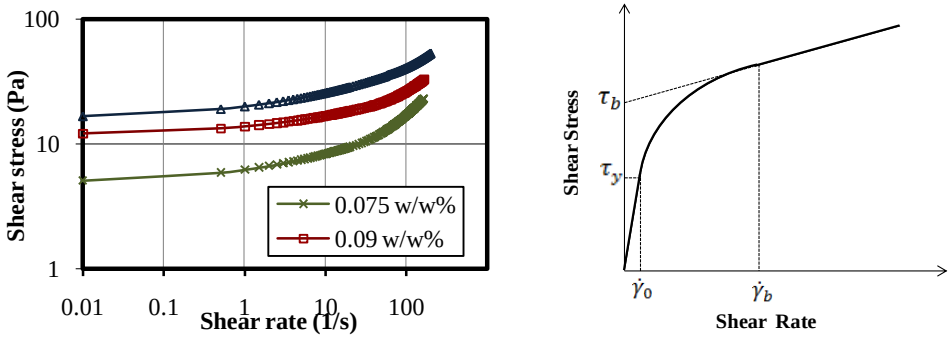

(a) (b)

Figure 5-2. (a) Flow curves of three carbopol solutions at different concentrations (b) Flow curve segmentation.

The fluid rheology was incorporated into the computational model using a user-defined function (UDF). The rheological model is presented in equation 5-1 and the parameters are given in Table 5-1.

$$\mu = \begin{cases} \frac{\tau_y}{\dot{\gamma}_0}, & \dot{\gamma} < \dot{\gamma}_0 \\ \frac{\tau_y + k\dot{\gamma}^n}{\dot{\gamma}}, & \dot{\gamma} < \dot{\gamma}_b \\ \frac{\tau_b + k_b\dot{\gamma}}{\dot{\gamma}}, & \dot{\gamma} \geq \dot{\gamma}_b \end{cases} \qquad 5\text{-}1$$

Table 5-1. Rheological parameters for the CFD model

(w/w%)	τ_y (Pa)	k (Pa.s^n)	n	τ_b (Pa)	k_b (Pa.s)	$\dot{\gamma}_0$ (s^{-1})	$\dot{\gamma}_b$ (s^{-1})
0.075	4.9±0.4	1.32	0.4	7.49	0.094	0.0001	25
0.09	10.8±0.8	1.99	0.4	16.4	0.1	0.0001	30
0.1	16±0.9	3.94	0.4	28.47	0.123	0.0001	37

5.2 Model evaluation

The fluid dynamics inside a stirred tank is strongly affected by a large number of variables. This generates some uncertainty on the application of mathematical models to predict mixing processes. Hence, the CFD results were compared with information obtained from particle image velocimetry (PIV) experiments to evaluate capabilities and limitations of the model. The results obtained from this experimental technique allow comparison of two components of the fluid velocity at specific locations, and large-scale flow patterns. The resolution of the CFD and PIV velocity fields is different, since an unstructured mesh with high density of elements around the impeller was used for the CFD model.

Velocity profiles at 2 vertical planes were used to evaluate the model. The plane Z=0, which shows the axial and radial components of the velocity at the center of the cavern, and the plane Z=5 that provides information on the flow pattern next to the blade tip. It can be observed from Figure 5-3 that excellent agreement exists between the model prediction (CFD) and experimentally obtained (PIV) flow patterns at 416 rpm. The circulation loops that drive the flow to the suction zones of the impeller and the distribution of velocities are well captured by the CFD model. High speed red vectors illustrate the impeller discharge and low speed blue vectors show zones of slow motion. Figure 5-3a (Z=0) shows the ability of the model to predict the axial-radial discharge of the impeller and the returning pattern to the suction zone behind the

impeller. Figure 5-3b (*Z*=5) shows that the high speed vectors located next to the blade are pointing upward, which reveals the strong tangential flow created by the viscous forces. Due to the shear thinning behaviour of the carbopol solutions, the strength of these forces is closely related to the rate of fluid deformation. The similarity of the flow patterns in Figure 5-3b reflects the capability of the CFD model to calculate the levels of shear rate around the impeller.

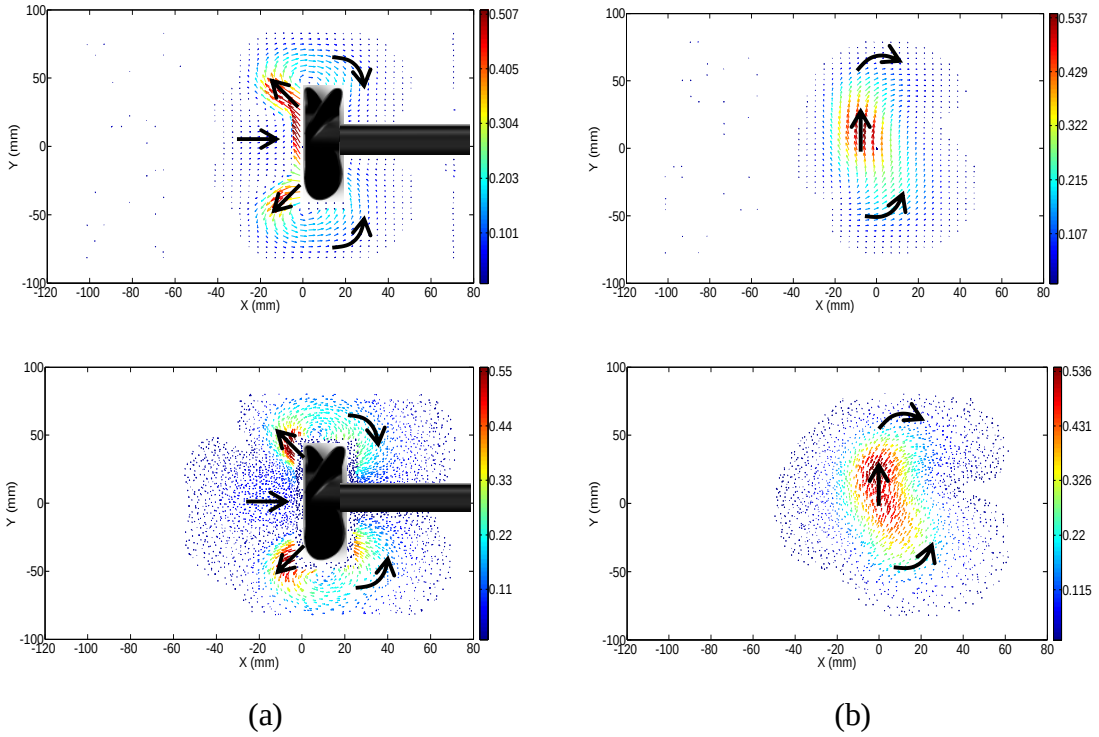

(a) (b)

Figure 5-3. Experimental (top) and CFD (bottom) 2D velocity field generated by the A100 impeller for a 0.1 w/w% carbopol solution at 416 rpm. (a) *Z*=0, (b) *Z*=5. Velocity vectors colored by velocity magnitude (m/s)

In the CFD model, the rheology does not include the yield stress as it is defined, but an extremely viscous fluid instead. Hence, the velocities predicted by the model for the dead zones are not zero as is in the real system, but are extremely low. The velocity fields shown in Figure 5-3 include only vectors with magnitudes over 0.01 m/s. This provides an idea of the shape and size of the pseudo-caverns formed around the impeller. There is a satisfactory agreement in the cavern size and shape between the modeling and experimental data. At both planes (*Z*=0 and *Z*=5), the silhouettes displayed by the boundary vectors of the model represent well the cavern shapes observed during the corresponding experiments. Pseudo-caverns can be used to examine active zones, when the exact localization of the cavern boundary is not of primary interest.

The performance of the model predicting the effect of the rotational speed is presented in Figure 5-4. This figure shows the velocity fields at *Z*=0 and *Z*=5 of a 0.1 w/w % carbopol solution at 684 rpm. By comparing the vector maps at the top of Figure 5-3 and Figure 5-4, it can be seen how the axial component of the discharge gains weight as the rotational speed increases. At 684 rpm, the inertial forces become more dominant and change the fluid direction in the discharge zone. This change in the discharge angle is clearly predicted by the CFD model (bottom part Figure 5-3 and Figure 5-4). Another significant difference between the two rotational speeds is the strength of the jets, and consequently the size of the cavern. As shown in Figure 5-4, the cavern boundary at 684 rpm was outside of the investigated area during the PIV experiments. However, the extent of the predicted jets at 684 rpm (at *Z*=0) is evidently larger compared to the ones at 416 rpm. At *Z*=5 (Figure 5-4b), the vector directions show how the flow drastically change the orientation. The strong tangential component of the velocity observed at lower velocities (416 rpm) vanishes, and axial flow arises instead. Although, the model over-predicts velocity values (up to 20%) in some regions, the shape of the high speed zones is well predicted. These zones are the backbone of the cavern, so a good cavern shape prediction is expected. At X=20 mm and Y=0 on plane *Z*=5, there is a strong vortex created by the suction behind the blade that is accurately predicted by the model.

The ability of the CFD model to reproduce the effect of impeller geometry and rheological properties is shown in Figure 5-5. This figure shows the velocity field at *Z*=0 generated by the A312 impeller at 684 rpm for a 0.09 w/w% carbopol solution. As seen in Figure 5-1, the blade angles of the A100 and A312 impellers are different, which causes reorganization of the flow structures. Moreover, the rheological parameters of the 0.09 w/w% solution generate a completely different distribution of viscosities in the mixing domain. The CFD model is able to capture the main characteristics of the flow under the new conditions. As in the case of the A100 impeller, the numerical solution of the governing equations replicates the discharge angle and the extent of the jets obtained from PIV trials. The location of the circulation loops created by the interaction of the discharge and suctions streams match the results obtained from PIV. It has been shown that the position of these recirculation regions is closely related to the Reynolds number. Thus, as the Reynolds number decreases, the loops created on the outer side of the jets shift towards the impeller (Chapter 4). Evaluations at different rotational speeds confirmed the capacity of the model to establish the ratio between the inertial and viscous forces.

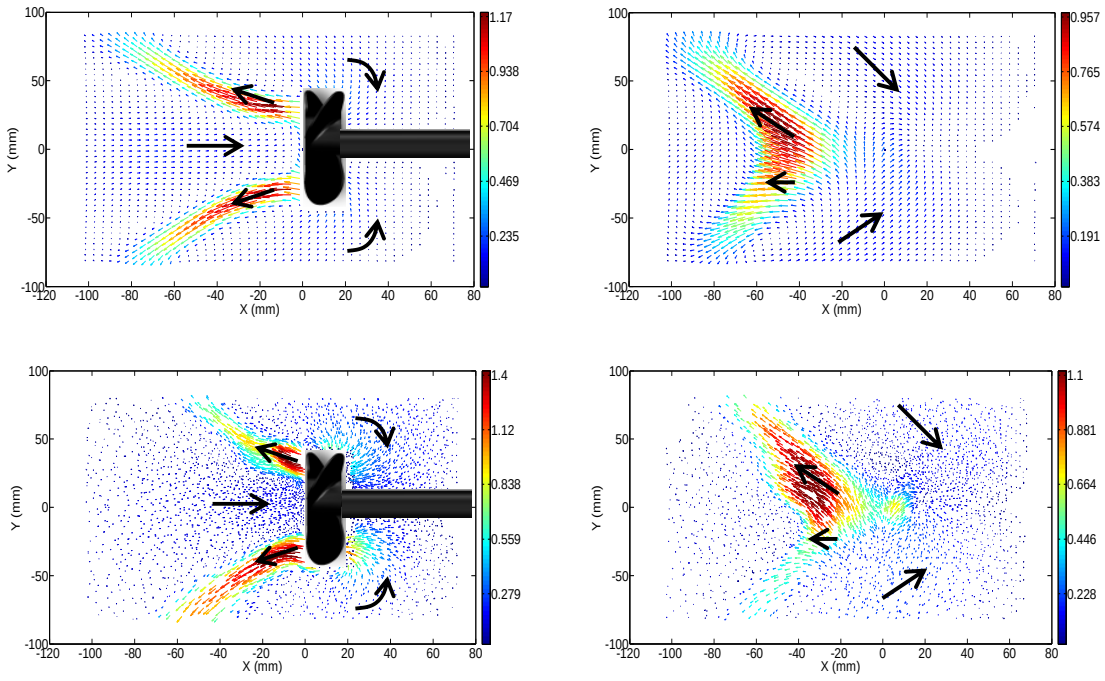

(a) (b)

Figure 5-4. Experimental (top) and CFD (bottom) 2D velocity field generated by the A100 impeller for a 0.1 w/w% carbopol solution at 684 rpm. (a) *Z*=0, (b) *Z*=5. Velocity vectors colored by velocity magnitude (m/s)

Computational results can be quantitatively evaluated by comparing velocity profiles along sample lines. Figure 5-6 shows the results of normalized velocities along a vertical sample line located 15 mm in front of the impeller on the plane *Z*=0. The peaks on the plots correspond to the velocities of the jets discharged by the impeller. The profiles in Figure 5-6a show the axial component of the velocity (*U*) over the sample line. Negative values belong to the flow going away from the impeller, and positive values refer to the suction streams. For the radial component of the velocity (V), the positive values indicate upward flow, and negative values the opposite flow (Figure 5-6b). The good match between the experimental and computational profiles of the radial and axial components implies a good prediction of the discharge angle. Also, the observed agreement of the velocity profiles crossing the zero velocity line means that the model precisely predicts the place where the flow changes its direction. The calculated velocity values are very satisfactory, particularly for the downward discharge. The maximum velocity over the sample line is below 20% of the tip speed (U_{tip}), which reflects the effect of the high viscosity. The disagreement of the profiles in the upper part ($Y^* \geq 0$) of Figure 5-6a and 5-6b is observed also on the velocity fields in Figure 5-3a. Although, the downward discharge is

very well represented, the radial component of the upper jet is a bit higher for the computed field.

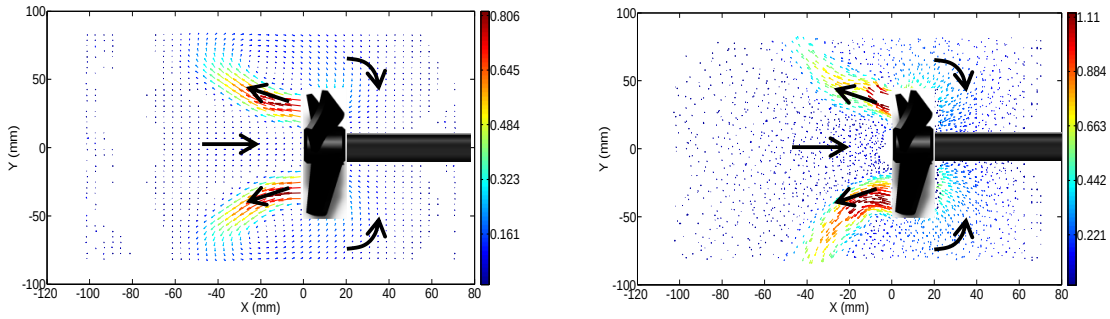

(a) (b)

Figure 5-5. Two dimensional velocity field at *Z*=0 generated by the A312 impeller for a 0.09 w/w% carbopol solution at 684 rpm. (a) Experimental, (b) CFD. Velocity vectors colored by velocity magnitude (m/s)

The profiles in Figure 5-6c show the normalized total velocity (*L**) along the sample line at 684 rpm. Again, the boundary between suction and discharge streams is well predicted by the model. The computed profile captures the flow structure in the discharge zone and provides velocity values with an error below 21%, compared to the PIV results. The predictions at locations below the shaft (Y*<0) at 684 rpm is not as good as the ones at lower angular speeds. Other flaws of the computed flow field at 684 rpm are evident in Figure 5-4a and 5-4b. The computed velocity field does not display the symmetry of the PIV results. That is, the extent of the upper jet is notably lower compared to its counterpart on the down side. This limitation is not clearly manifested at 416 rpm (figures 5-3a), so it can be stated that this flaw becomes more notorious as the angular speed increases.

The incapability of the CFD model to calculate the symmetric flow shown in experimental results lies on the approach used to model the rotation of the impeller. The MRF approach provides a steady state result for one specific impeller position, but ignores the flow history. That is, the computed flow pattern does not consider the flow generated when the impeller blade was in other positions. The impeller position during the PIV measurements matches the impeller position in the model. However, the results are different because the experimental approach includes the inertial motion created by the pass of the blades above the shaft, which increases the upward discharge. The effect of these inertial forces on the flow pattern becomes more notorious as the angular speed increases. Hence, the pattern at high speeds would be like the one created

by an impeller with infinite number of blades. Flow under this condition might not display the periodic fluctuation generated by the pass of the impeller blades, which explains why the mixing can be better at low Reynolds number as shown by Zalc et al., (2002).

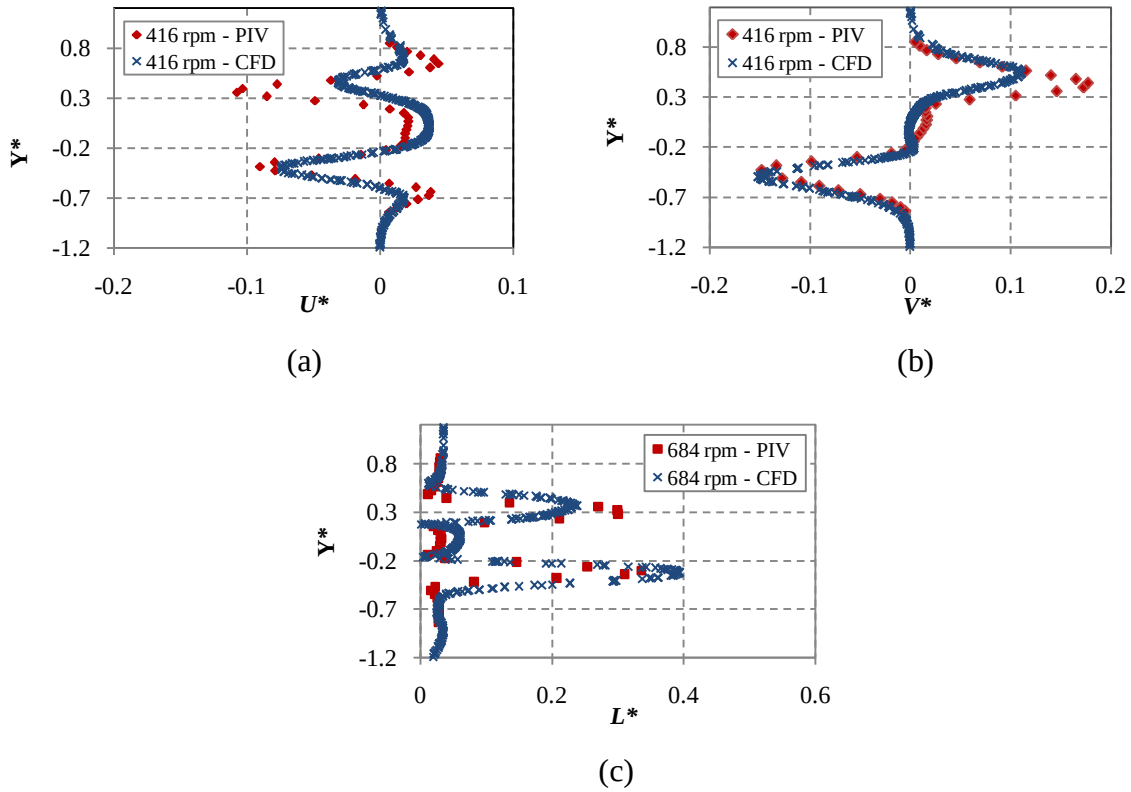

Figure 5-6. CFD and PIV results of normalized velocities along a sample line located 15 mm in front of the impeller on the plane *Z*=0. (a) Horizontal component of the velocity (*U*) at 416 rpm. (b) Vertical component of the velocity (*V*) at 416 rpm. (c) Total velocity (*L*) at 684 rpm.

The fact of ignoring the flow history at high angular speeds mainly affects the flow prediction in-between two consecutive blades. Figure 5-7 shows the 120˚ rotational symmetry of the flow pattern generated by the CFD model if the interaction of the flow with the vessel walls is negligible. The figure also shows how the strong jet would come out from the upper jet if the impeller position is turned 180˚ degrees, which discards the possibility of having an asymmetric flow field due to the relative position of the impeller with respect to the tank walls.

The numerical solution of the governing equations is able to estimate critical features of the flow such as pseudo-caverns, location of circulation loops and reasonable velocity values. The MRF approach is suitable for cases where an overall idea of the flow or/and characteristic parameters (e.g. power requirements or pumping capacity) are sought.

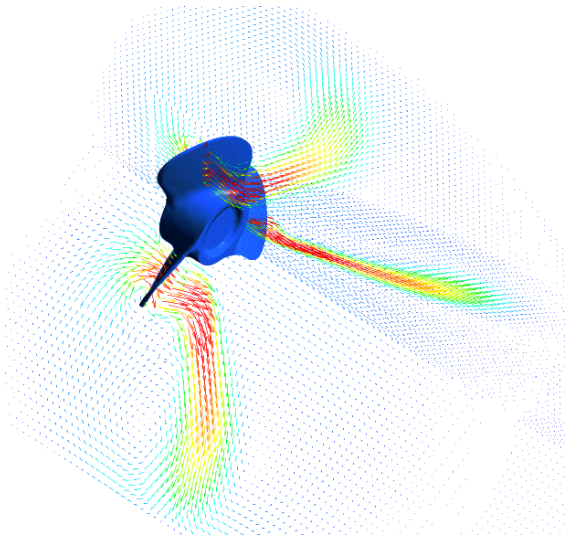

Figure 5-7. 120˚ rotational symmetry of the flow pattern.

5.3 Characterization of the mixing hydrodynamics using the developed model

The results of the CFD model were used to compare mixing characteristics of the three impellers and the three carbopol solutions. The evaluation includes: Flow structure, segregated regions, shear rate distributions, pseudo-cavern size and shape, pumping number and power number at different operating conditions.

As observed before, the flow pattern at the discharge zone depends on the operating conditions. Thus, at different angular speeds or different viscosity values, the impeller discharge might vary from radial to axial. The discharge angle directly affects the size and the shape of the active zone. Figure 5-8, shows velocity isosurfaces created at 0.4 m/s for the A100 impeller at different operating conditions. The boundaries displayed by these isosurfaces do not show the limit of the cavern, but the structure of the impeller discharge instead. At low rotational speed (327 rpm) and high concentration (0.1 w/w%), the axial discharge is weak and the flow is mainly tangential (Figure 5-8a). Therefore, the viscous forces create a flow structure with a toroidal shape, where two main flow patterns co-exist. Part of the fluid in motion belongs to the fluid pumped by the impeller that promptly returns to the suction zone behind the blades, and the other part travels around the impeller without significant changes in flow direction. At a higher angular speed (684 rpm), there is a reorganization of the flow structure due to the increase of the axial discharge (Figure 5-8b). The conical blue structure embodies the outward pumping action of the impeller.

The three tips observed at the end of the cone correspond to the strong jets discharged by each blade, which are accentuated in the numerical results due to the MRF approach used to model the impeller rotation. However, a more circular end for this cone is expected under real mixing conditions. The isosurface created at 0.4 m/s roughly shows the frontier between the discharge and suction streams. The returning flows displayed in the velocity fields of Figure 5-4a are located inside and outside of this conical configuration. Unlike the flow at low rotational speed, most of the fluid goes through the blades and constantly changes its direction. A similar flow distribution is observed in Figure 5-8c, when mixing a more dilute solution (0.075 w/w%) at a lower rotational speed (416 rpm). Although, the rotational speed is lower, there is a predominant axial discharge due to the lower viscosity. The pattern describes again a conical discharge region with a comparable size. It is presumed that the similar flow arrangement can potentially be achieved for two different carbopol solutions by modifying the rotational speed, i.e. the flow structure is dictated by the Reynolds number.

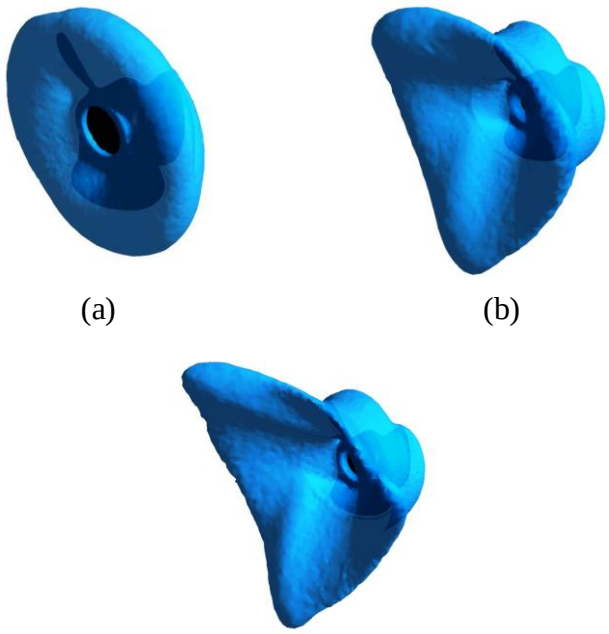

Figure 5-8. Velocity isosurfaces at 0.4 m/s for the A100 impeller. (a) 0.1 w/w% at 327 rpm. (b) 0.1 w/w% at 684 rpm. (c) 0.075 w/w% at 416 rpm.

The ratio of inertial and viscous forces depends on impeller geometrical properties. Thus, for different blade angles and shapes the pumping capacity and the flow direction vary considerably. The characteristic pitch ratio of the three impellers under study defines the axial thrust imparted

in the discharge zone of the impeller, thereby creating active zones with different properties. The pseudo-caverns formed by the three impellers are presented in Figure 5-9. The criteria used to find the cavern boundary was a minimum velocity of 0.001 m/s, which is less than 0.1% of the tip speed in this case (416 rpm). It can be observed that differences in size and shape exist between the three. The cavern volumes are 25%, 14% and 10% of the tank volume for the A100, A312 and Maxflo Mark II impellers, respectively. As the pitch ratio increases, the cavern growth in the axial direction becomes more relevant. Thus, the cavern of the A100 (Figure 5-9a) impeller displays a more even enlargement in the axial and radial directions, thereby rendering an ellipsoid shape cavern. On the other hand, at the same operating conditions, the prevailing radial discharge imparted by the Maxflo impeller (Figure 5-9c) creates toroidal shape caverns.

The mathematical models available in the literature to predict cavern sizes have been derived assuming specific cavern shapes (Elson et al., 1986; Amanullah et al., 1998 and Adams and Barigou, 2007). A wide variety of geometries including cylindrical, spherical, and toroidal, among others have been used, with acceptable results compared to experimental observations. However, it is believed that these expressions are applicable to a very narrow range of mixing conditions, since the results presented so far show that the cavern size and shape are strongly related to the discharge angle and strength. These flow properties in turn depend on the blade angle, the impeller position, the rheologial properties and the operating conditions (chapters 3 and 4).

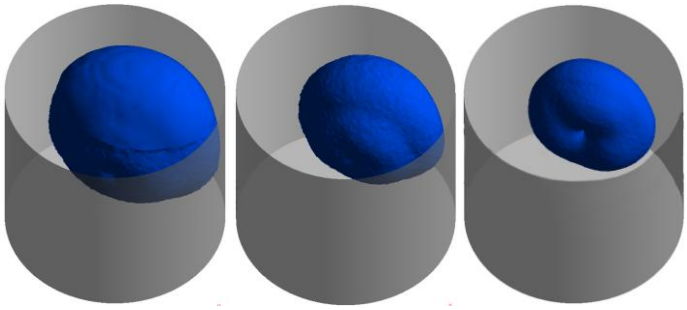

(a) (b) (c)

Figure 5-9. Pseudo-caverns (velocities over 0.001 m/s) for a 0.1 w/w% carbopol solution at 416 rpm using the (a) A100, (b) A312 and (c) Maxflo Mark II impeller.

The previous section shows the capability of the CFD model to predict the circulation loops created by interaction between the outward and inward streams. Previous studies on mixing have revealed the formation of similar patterns along with their characteristics (Lamberto et al., 1999; Lamberto et al., 2001 and Zalc et al., 2002).). It was shown that these regions have little or no material exchange with the bulk flow. Thus, it was meant in this study to investigate the characteristic of the predicted loops by plotting three dimensional streamlines inside these regions. The streamlines show the path followed by massless particles through the fluid domain. The starting point of the streamlines was selected on the bottom-half of the plane Z=0, since the circulation loops are clearly identified in the velocity fields of this plane. An example of the position of the initial point is shown by the red cross in Figure 5-10.

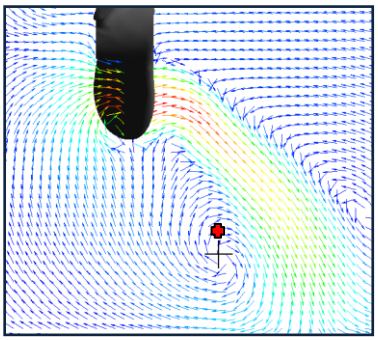

Figure 5-10. Initial point for three dimensional streamlines

Figure 5-11a shows the streamlines for the A100 impeller at 565 rpm in the 0.1 w/w% carbopol solution. Two different views of the path lines are presented. The lateral view clearly shows that the particle does not flow to the suction zones of the impeller, and follows almost the same path around the impeller instead. This suggests that there is little material exchange between this region and the main circulation loops. From the front view in Figure 5-11a, it can be observed that the isolated region has a triangular shape. However, this explicit form might be a characteristic result of the MRF approach used in this model. It is believed that under real conditions this region has a more circular shape, resembling segregated toroidal regions found in other studies.

In order to evaluate the effect of the mixing conditions on the formation of these enclosed regions, similar streamlines were plotted for the A312 impeller at 684 rpm in the 0.09 w/w% carbopol solution (Figure 5-11b). Despite the differences, the result was very similar to the segregated region presented in the previous case. The path follow by the particles does not pass

through the blades at any time. A visible difference between the two mixing conditions is the location of the recirculation loops, which are dependent on the Reynolds number. For the conditions used with the A312 impeller, the segregated region is closer to the impeller, and it is inclined to the right due to the lack of symmetry of the recirculation loops (observed in the computed velocity field, Figure 5-5b). At very low Reynolds numbers the recirculation loops tend to disappear. The quasi-radial discharge displayed at these conditions might be so weak that the suction stream becomes a continuation of the discharge stream (Chapter 4). Hence, the onset of segregated regions is conditioned to the existence of a large enough discharge that allows the outward flow entrains fluid from the opposite streams. During the flow visualization experiments, recirculation loops in the inner part of the conical structures presented in Figure 5-8 were also observed. These loops would be the result of the interaction between the discharge and the stream flowing to the center of the impeller. However, streamlines computed by the CFD model were not able to confirm the existence of isolated regions inside the conical structures. This inability of the model might be due to the asymmetric flow computed by the MRF approach. Hence, this flaw could be overcome using a time-dependent methodology to model impeller rotation.

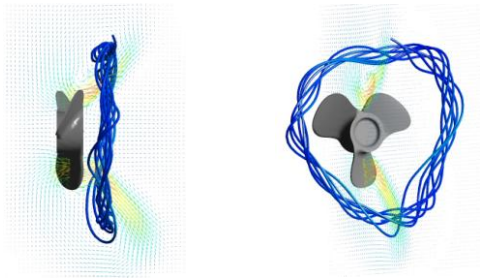

(a)

(b)

Figure 5-11. Closed streamlines in segregated regions. (a) A100 impeller at 565 rpm in the 0.1 w/w% carbopol solution, (b) A312 impeller at 684 rpm in the 0.09 w/w% carbopol solution.

The optimum design and operation of stirred tanks when mixing highly sensitive shear rate fluids, demands a comprehensive characterization of the shear levels around the impeller. Therefore, the shear rate distribution generated by the three impellers under study was examined at different regions in the mixing domain. The effective strain rate ($\dot{\gamma}$ in Equation 5-2) experienced by the fluid is spatially derived from the second invariant of the strain rate tensor at specific locations.

$$\dot{\boldsymbol{\gamma}} = \left[\frac{\mathbf{1}}{\mathbf{2}}\bar{\bar{\boldsymbol{D}}}:\bar{\bar{\boldsymbol{D}}}\right]^{\mathbf{1/2}} \qquad 5\text{-}2$$

Figure 5-12 shows the shear rate contours on plane Z=0 generated by the three impellers for a 0.1 w/w% carbopol solution at 565 rpm. To make the comparison easier, the three contours were plotted using the same scale of shear rates (0.1-100 s^{-1}). However the highest shear rates computed on that plane are 1376, 1397 and 1530 s^{-1} for the A100, A312 and Maxflo, respectively. As expected, the zones with the highest rates of deformation are created by the trailing vortices (generated by the rotating blades), and are located in the vicinity of the impeller. The wider red area observed for the A100 impeller (Figure 5-12a) around the blade placed below the shaft is directly related to its pitch ratio. For the other two impellers, the lower pitch ratios make the area covered by the trailing vortices smaller. The flow generated by the A100 impeller (Figure 5-12a) also exhibits the formation of high shear zones (barely observed for the other two impellers) in the axial direction. The observed flow direction in the velocity fields of the A100 impeller, suggests that the rate of deformation is boosted in the surroundings of the discharge path. The A312 impeller discharge also creates a high shear rate zone (Figure 5-12b). However, it is much smaller compared to that of the A100 impeller, and it expands more towards the bottom wall of the vessel. In the case of the Maxflo impeller (Figure 5-12c), the area of high shear rate is restricted to the region affected by the tangential motion of the fluid. From these results, it can be stated that the shear rate contours resemble the flow structure generated by each impeller. The boundary displayed by the biggest contour (low shear rate) in the three figures provides an idea of the lateral view of the cavern generated by each impeller.

Due to the nature of the fluid used in this study, an idea of the viscosity distribution can be derived from the shear rate contours. Relatively speaking, low viscosities are expected close to the impeller walls and all along the discharge stream. The viscosity increases as the fluid goes away from the impeller. The suction streams experience high viscosities up to a point, where the low pressure zone created behind the blades accelerates the rate of deformation, and drops the

viscosity again. The extended discharge of the A100 impeller creates a large zone of low viscosities; however there is also a significant portion of the active zone (mainly suction streams) with high viscosities due to the low shear rates underwent by the fluid. The average shear rates calculated inside the cavern (The cavern boundary was defined by a minimum velocity equals to 0.001 m/s) on the plane Z=0 are 11.13, 15.21 and 11.6 s^{-1} for the A100, A312 and Maxflo, respectively. Although, the discharge zone of the A100 impeller offers a larger area with high shear rates, the A312 impeller provides the highest average shear rate.

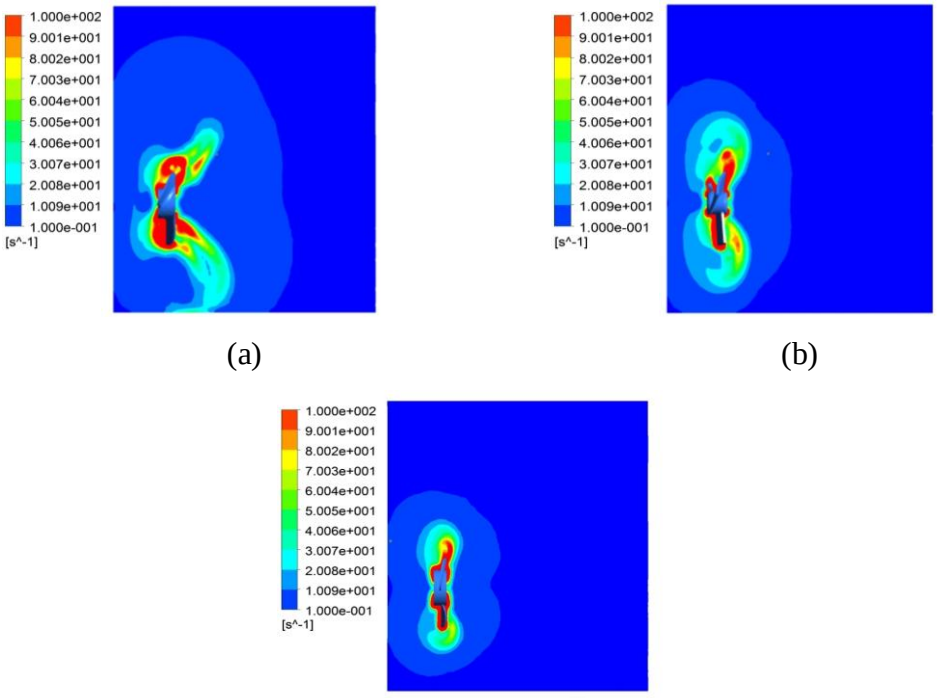

Figure 5-12. Shear rate contours on plane Z=0 of a 0.1 w/w% carbopol solution at 565 rpm. (a) A100 impeller, (b) A312 impeller, (c) Maxflo Mark II impeller. Zones with shear rates higher than 100 s^{-1} are colored in red and lower than 0.1 s^{-1} are colored in dark blue.

Similar flow characteristics can be observed at different operating conditions (416 rpm), and on a different plane. Figure 5-13 presents the shear rate contours on a plane YZ placed 10 mm in front of the impeller with some transparency to show the impeller blades position. Localized high shear rate zones (red areas) can be observed for the A100 impeller (Figure 5-13a). These three regions show the high shear rate generated by the pass of the jets released by the impeller through this plane. The relative position of these areas with respect to the blades gives an idea of

the tangential component of the impeller discharge. The contours for the A312 impeller (Figure 5-13b) show that the shear rate is more uniformly distributed, with large zones of medium-high shear rate values. The absence of localized zones with high shear rates means that most of the impeller discharge is passing tangential to the plane. In the case of the Maxflo impeller (Figure 5-13c), the axial discharge is almost negligible and the strong tangential component of the flow creates the highest shear rate zone in the periphery described by the blade tip rotation. The average shear rates calculated on the YZ plane at X=10 mm are 12.7, 15.4 and 12.2 s^{-1} for the A100, A312 and Maxflo, respectively. Again, the highest average belongs to the A312 impeller. Although, the A100 has the largest values of shear rate, the large area occupy by the returning flow (low shear rates) brings down the average.

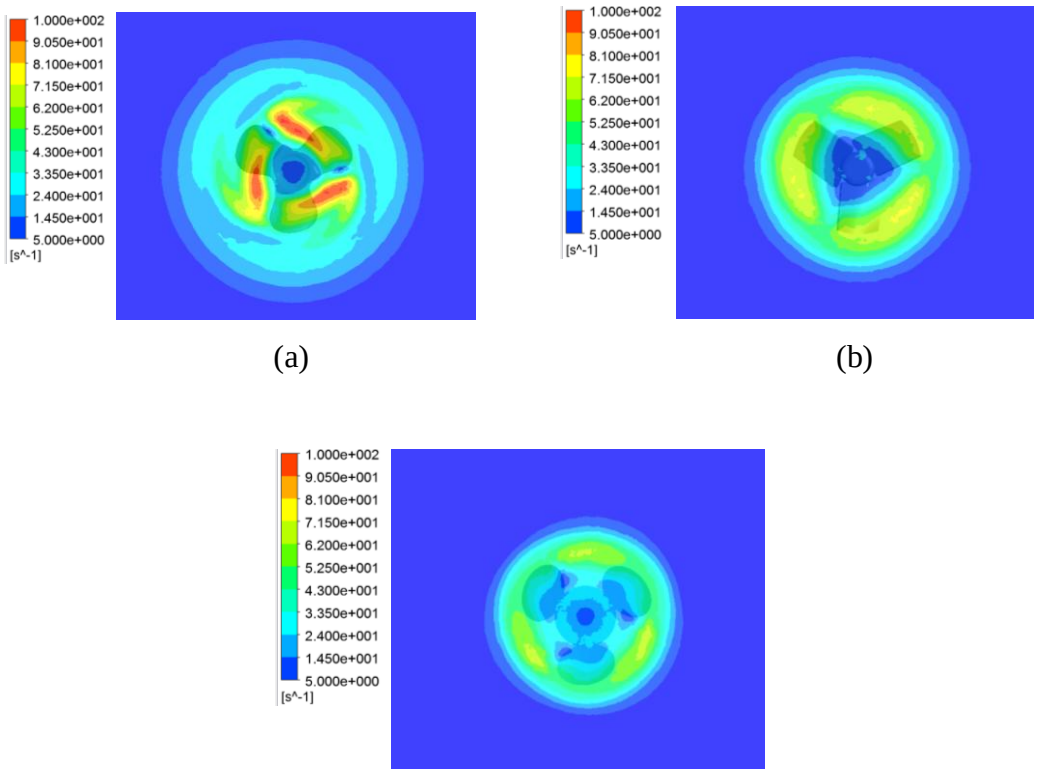

Figure 5-13. Shear rate contours on plane located 10 mm in front of the impeller for a 0.1 w/w% carbopol solution at 565 rpm. (a) A100 impeller, (b) A312 impeller, (c) Maxflo Mark II impeller. Zones with shear rates higher than 100 s^{-1} are colored in red and lower than 0.1 s^{-1} are colored in dark blue.

A spatial distribution of the shear rate was constructed by evaluating the volume fraction of the cavern undergoing a specific shear rate. The shear rate levels were plotted against the normalised

volume (equation 5-3), where $v_{\dot{\gamma}}$ is the volume of a fluid element with shear rate $\dot{\gamma}$, and V_c is the cavern volume.

$$\overline{V_{\dot{\gamma}}} = \frac{\sum v_{\dot{\gamma}}}{v_c} \qquad 5\text{-}3$$

The distribution is presented in Figure 5-14. The largest volume fraction computed for the A100 at low shear rates is in agreement with the low shear rate areas previously identified in the contours of this impeller. Although, the shear levels are very similar for the three impellers, the A312 provides the most uniform distribution. This consistency in the distribution keeps the average shear rate above the ones for the other two impellers. The shear rate volume-weighted average for the A100, A312 and Maxflo are 6.0, 7.9 and 5.9 s^{-1}, respectively. Thus, the lowest average viscosity in the active zone is generated by the A312 impeller. These findings can be extrapolated to other rotational speeds and fluid rheologies.

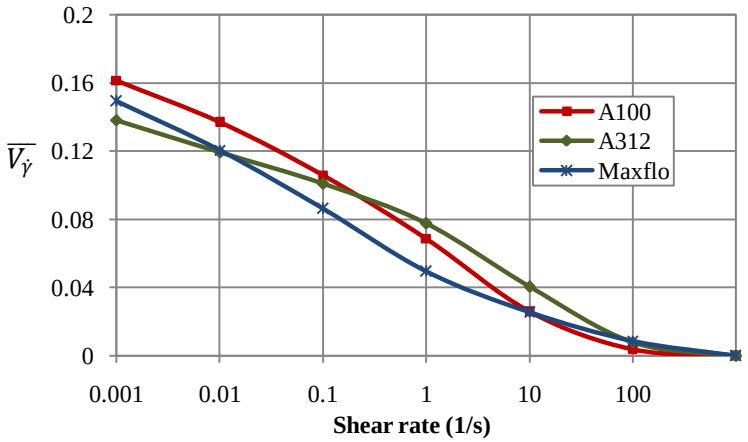

Figure 5-14. Spatial shear rate distribution at 327 rpm for a 0.1 w/w% carbopol solution

The performance of the three impellers was characterized by computing the power and pumping numbers under different conditions. The Power number (N_p) was calculated from equation 1-2. The power draw (P) was computed from the torque exerted on the impeller walls with respect to the x-axis.

The pumping number (N_q) was calculated from equation 1-4. The flow rate (Q) was calculated from the mass flow crossing a circular surface with diameter D (impeller diameter), and placed 7 mm in front of the impeller. The disk surface was clipped to exclude the central area, where the flow is returning to the impeller

Illustrations of the outflow and inflow areas are shown in Figure 5-15 (Countours of the x-velocity for the three impellers for a 0.1 w/w% carbopol solution at 416 rpm). The triangles in the center show the area of the returning flow (negative values of the x-velocity), while the external parts show the outflow areas. The snapshot approach used to model the impeller rotation shows how the top values are concentrated in the three zones in front of the blades. It is seen that the A100 impeller has the highest velocity values (blue area) for the outflow. The strong axial discharge of this impeller increases the pumping capacity as previously defined. The area-weighted average of the velocity drops as the pitch ratio decreases. Thus, the impeller with the lowest outflow capacity is the Maxflo. It is shown in Figure 5-15c how this condition creates also the largest inflow area.

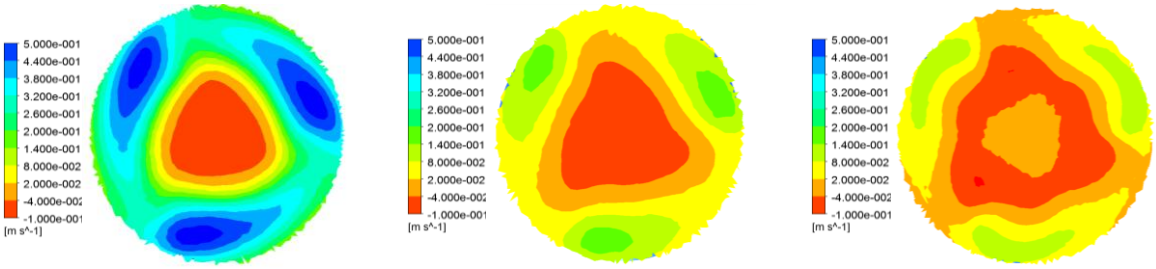

Figure 5-15. x-Velocity contours on circular plane (Diameter = 9.652 cm) located 5 mm in front of the impeller in a 0.1 w/w% carbopol solution at 416 rpm. (a) A100 impeller, (b) A312 impeller, (c) Maxflo Mark II impeller. The negative values (red) show the returning flow, while the positive values (blue) show the outflow.

The N_p and N_q parameters were evaluated for different combinations of angular speed and carbopol concentration. The results are presented in Figure 5-16. The curves generated by each impeller in different carbopol solutions nearly fall into a single operating curve, when the yield stress Reynolds number (Equation 3-1) is used in the horizontal axis. This would not be the case if the conventional Reynolds number for mixing systems (Equation 1-1) is used instead. The curves show that the operating conditions evaluated in this study produce an overall flow within the laminar and transitional regimes. The curves of the A100 impeller reach asymptotic values at lower Reynolds Numbers compared to the curves of the other two impellers. That is, the enhanced axial thrust imparted by this impeller drives the flow to the turbulent regime at milder operating conditions. The conditions at the tail of the curves correspond to the lowest concentration (0.075 w/w%) and the highest angular speed (684 rpm). Under these conditions, turbulent flow might exist in the vicinity of the impeller.

The curves show the positive correlation found in other studies (Kumaresan and Joshi, 2006 and Bhole and Bennington, 2010) between the pitch ratio and the pumping capacity and the power consumption. A general assessment of the computed values against experimental measurements of N_p and N_q presented in Chapter 4 (dash lines in figure 5-16), shows that the power requirements are well predicted by the CFD model, and the pumping capacity is over-predicted by 30% (average) of the experimental value. The largest deviations are observed at the lowest Reynolds number.

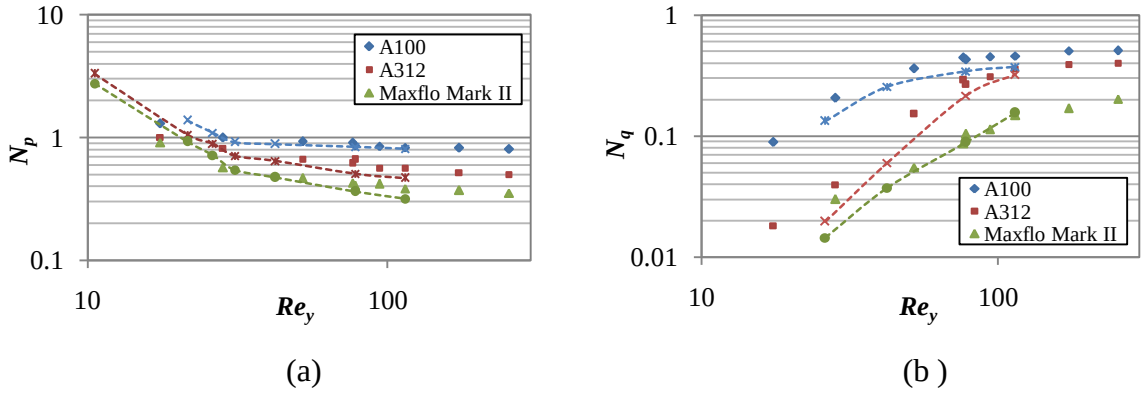

Figure 5-16. Impellers characterization. Discontinuous points show the computational prediction and dash lines show experimental values reported in Chapter 1. a) N_p vs. Re_y. b) N_q vs. Re_y.

6. Conclusions and recommendations

6.1 Conclusions

The effects of clearance, vessel shape, and impeller type on the hydrodynamics of non-Newtonian fluids were evaluated using particle image velocimetry (PIV). The different flow structures revealed that the ratio of inertial and viscous forces largely defines the flow pattern. Due to the shear thinning behaviour of the non-Newtonian fluids, the viscous forces are very sensitive to the shear rate distribution of each mixing configuration. High impeller pitch ratios improve the impeller discharge, thereby providing a dominantly axial flow and a larger mixing volume. In the same manner, the suction area defined by the clearance and vessel shape, determines the inertia on the flow ejected by the impeller. By this principle, it conditions the extent of the active zone in the axial and radial directions.

The flow patterns indicated the importance of the impeller position in side-entry impeller configurations. The results point out that an optimum vertical location of the impeller is required so that the extent of the mixing zone is not deteriorated by a flow restriction to the suction zone below the shaft. Thus, when the bottom wall is too close to the blades the extent of the downward discharge is shorter compare to that of the upward counterpart. This flow restriction arises when the boundary imposed by the yield stress is beyond the vessel walls.

The vector fields showed the response of the flow circulation at different viscosities. In the case of Glycerin, the high viscous forces present in the entire mixing domain inhibit the axial discharge. Therefore, part of the fluid follows concentric closed stream lines around the impeller, which deteriorates the mixing quality. On the other hand, the shear thinning behaviour of the carbopol solutions provides a wide distribution of viscosities around the impeller. Close to the impeller blades the viscosity can be low enough that the inertial forces are able to impose axial flow. As the Reynolds number increases the discharge angle approaches a constant value, and the fluid follows the same path around the impeller regardless of the angular speed.

The interaction between the discharge and suction streams of the impellers creates self-circulating zones that are re-allocated with changes in the Reynolds number and tend to disappear for small cavern volumes. Three dimensional streamlines initiated at the center of these self-circulating structures, and high dye concentrations in these regions suggest that the material exchange of these zones with the main circulation loops is very limited. The revealed

structures resemble segregated toroidal zones reported in the literature for other mixing configurations.

The computational fluid dynamic (CFD) models were able to predict the effects of impeller properties (blade angle) and rheological characteristics (yield stress and variable viscosity) on the axial, radial and tangential components of the discharge, the location of re-circulation loops and the power requirements under a wide range of operating conditions. However, the flow symmetry displayed in experimental results was not captured by the computational results. It is believed that the implicit condition of the moving reference frame technique of ignoring flow history limits the prediction of some flow properties, especially at high angular speeds.

The modeling results indicated that the structure of the discharge flow (affected by rheology, blade angle and operating conditions) dictates the cavern size and shape. As the radial component of the discharge increases, the returning flow through the center of the impeller decreases and the cavern adopts a toroidal form. On the other hand, a large axial discharge provides relatively larger caverns with ellipsoidal shapes.

Experimental and numerical results show that for the impeller with the smallest pitch ratio, the power requirements and the pumping capacities were lower compared to those of the impellers with larger pitch ratios. The evaluated N_p and N_q numbers were plotted against the yield-stress Reynolds number in order to report single operating curves for each impeller. It was found that the impeller with the largest pitch ratio offers the largest cavern volume and localized high shear rate regions. Although, the shear levels generated by the three impellers are very similar, the results show that the spatial distribution of the shear rate is determined by the path of the impeller discharge.

6.2 Recommendations for future work

Evaluate the rates of stretching and folding of fluid elements in the mixing domain to determine if distinctive properties of chaotic mixing are present. Two alternatives to identify chaotic regions are 1) Poincaré sections, which are two-dimensional maps (usually on planes perpendicular to the main flow direction) that show the area visited by tracer particles over time, and 2) Stretching fields, which measure the elongation experienced by fluid elements.

It is believed that during the repositioning of the segregated zones (generated by changes in the rotational speed) the material enclosed in these zones is substituted by new material. Dynamic PIV measurements of the flow generated immediately after changing the rotational speed can provide information on this statement. The instant velocity maps would show how the flow structures release the segregated material to the bulk flow and segregate new material as the flow adopts the new pattern.

Dye can be injected inside the segregated zones (identified inside and outside of the discharge stream) to experimentally confirm the weak interaction between the fluid trapped in these zones and the main circulation loops. This would also reveal the three-dimensional structure of these regions.

The implementation of the unsteady state form of the Navier-Stokes equations in the CFD model can provide information on the transient flow created by the pass of the impeller blades at specific locations. This can show how the periodic fluctuations (which enhance mixing) behave at different rotational speeds. The time-dependent solution of the flow would also allow us to confirm if the differences between the experimental and computational results obtained in this study are linked to the Moving Reference Frame (MRF) approach.

Laminar flow was assumed in the entire mixing domain of the CFD models. However, turbulent conditions might arise close to the blades, especially at high rotational speeds and low carbopol concentrations. Hence, a more elaborated model including both turbulent and laminar models can be implemented to possibly improve the prediction of the mixing variables.

References

Adams LW, Barigou M. CFD Analysis of Caverns and Pseudo-Caverns Developed During Mixing of Non-Newtonian Fluids. *Chem. Eng. Res. Des*. 2007; 85(5): 598-604.

Adrian R. Particle-Imaging Techniques for Experimental Fluid-Mechanics. *Annu. Rev. Fluid Mech.* 1991; 23(1): 261-304.

Amanullah A, Hjorth SA, Nienow AW. A new mathematical model to predict cavern diameters in highly shear thinning, power law liquids using axial flow impellers. *Chem. Eng. Sci.* 1998; 53(3): 455-469.

Annearchard D, Marouche M, Boisson H. Hydrodynamics and Metzner–Otto correlation in stirred vessels for yield stress fluids. Chem. Eng. J. 2006; 125(1): 15-24.

Arratia PE, Kukura J, Lacombe J, Muzzio FJ. Mixing of Shear-Thinning Fluids with Yield Stress in Stirred Tanks. AIChE Journal. 2006; 52(7): 2310-2322.

Bakker A, Myers KJ, Ward RW, Lee CK. The laminar and turbulent flow pattern of a pitched blade turbine. Chem. Eng. Res. Des. 1996; 74: 485-491.

Bakker A, Gates LE. Properly choose mechanical agitators for viscous liquids. Chem. Eng. Pro. 1995; 91(12): 25-34.

Barnes HA, Nguyen QD. Rotating Vane Rheometry — a Review. *Science*, 2001; 98:1-14.

Bhole MR, Bennington CPJ. Performance of Four Axial Flow Impellers for Agitation of Pulp Suspensions in a Laboratory-Scale Cylindrical Stock Chest. *Ind. Eng. Chem. Res.* 2010; 49(9): 4444-4451.

Bhole MR, Ford C, Bennington CPJ. Characterization of axial flow impellers in pulp fibre suspensions. *Chem. Eng. Res. Des.* 2009; 87(4): 648-653.

Bhole MR, Hui LK, Gomez C, Bennington CPJ, Dumont GA. The Effect of Off-wall Clearance of a Side-entering Impeller on the Mixing of Pulp Suspensions in a Cylindrical Stock Chest. *Can. J. Chem. Eng.* 2011*;* 9999: 1-11.

Bugay S, Escudié R, Liné A. Experimental Analysis of Hydrodynamics in Axially agitated Tank. *AIChE Journal*. 2002; 48(3): 463-475Chhabra RP, Richardson JF. *Non-Newtonian Flow and Applied Rheology*, Second edition. Burlington, MA: Esevier, 2008.

Chhabra RP, Richardson JF. *Non-Newtonian Flow and Applied Rheology*, Second edition. Linacre House, Jordan Hill, UK: Elsevier, 2008.

Couerbe G, Fletcher D, Xuereb C, Poux M. Impact of Thixotropy on Flow Patterns Induced in a Stirred Tank: Numerical and Experimental Studies. *Chem. Eng. Res. Des*. 2008; 86(6):545-553.

Curran SJ, Hayes RE, Afacan A, Williams MC, Tanguy P. Properties of carbopol Solutions as Models for Yield-Stress Fluids. *J. Food Sci.* 2002; 67(1):176-180.

Elson TP, Cheesman DJ, Nienow AW. X-Ray Studies of Cavern Sizes and Mixing Performance with Fluids Possessing a Yield Stress. *Chem. Eng. Sci*. 1986; 41(10): 2555-2562.

Ford C. CFD simulation of mixing dynamics in agitated pulp stock chests, M.A.Sc. thesis, 2004, University of British Columbia, Vancouver, Canada.

Gomez C, Bennington CPJ, Taghipour F. Investigation of the Flow Field in a Rectangular Vessel Equipped With a Side-Entering Agitator. *J. Fluids Eng.* 2010a; 132(5): 1-13.

Gomez C, Derakhshandeh B, Hatzikiriakos SG, Bennington CPJ. carbopol as a Model Fluid for Studying Mixing of Pulp Fibre Suspensions. *Chem. Eng. Sci*. 2010b; 65(3):1288-1295.

Hemrajani RR, Tatterson GB. *Mechanically Stirred Vessels*. In: Paul EL, Atiemo-Obeng VA, Kresta SM, editors. *Handbook of Industrial Mixing*. Hoboken, NJ: Wiley-Interscience, 2004.

Hui L, Bennington CJP, Dumont G. Cavern formation in pulp suspensions using Side entering axial-flow impellers. *Chem. Eng. Sci*. 2009; 64(3): 509-519

Ihejirika I, Ein-Mozaffari F. Using CFD and Ultrasonic velocimetry to Study the Mixing of Pseudoplastic Fluids with a Helical Ribbon Impeller. *Chem. Eng. & Tech.* 2007; 30(5): 606-614.

Jaworski Z, Nienow AW, Dyster KN, An LDA Study of the Turbulent Flow Field in a Baffled Vessel. *Can. J. Chem. Eng*. 1996; 74:3-15.

Kehn RO. Comparing top entry versus side entry agitator performance in low viscosity blending. *Can. J. Chem. Eng*. 2011; 89: 1059-1067

Keane RD, Adrian RJ. Theory of Cross-correlation Analysis of PIV Images. *Appl. Sci. Res*. 1992; 49:191-215.

Kelly W, Gigas B. Using CFD to Predict the Behavior of Power Law Fluids Near Axial Flow Impellers Operating in the Transitional Flow Regime. *Chem. Eng. Sci.* 2003; 58(10): 2141-2152.

Kelly W, Humphrey A. Computational fluid dynamics model for predicting flow of viscous fluids in a large fermentor with hydrofoil flow impellers and internal cooling coils. *Biotechnol. Progr*. 1998; 14(2): 248-58.

Khopkar A, Aubin J, Rubio-Atoche C, Xuereb C, Le Sauze N, Bertrand J, Ranade VV. Flow Generated by Radial Flow Impellers : PIV Measurements and CFD Simulations. *Int. J. Chem. Reactor Eng.* 2004; 2(A18): 1-17.

Kumaresan T, Joshi J. Effect of Impeller Design on the Flow Pattern and Mixing in Stirred Tanks. *Chem. Eng. J.* 2006; 115(3): 173-193.

Lamberto DJ, Alvarez MM, Muzzio FJ. Experimental and computational investigation of the laminar flow structure in a stirred tank. *Chem. Eng. Sci*. 1999; 54: 919-942.

Lamberto DJ, Alvarez MM, Muzzio FJ. Computational analysis of regular and chaotic mixing in a stirred tank reactor. *Chem. Eng. Sci*. 2001; 56(16): 4887-4899.

Lamberto DJ, Muzzio FJ, Swanson PD, Tonkovich AL. Using time-dependent RPM to enhance mixing in stirred vessels. *Chem. Eng. Sci.* 1996; 51(5): 733-741.

Magnin A, Piau JM. Cone-and-plate Rheometry Study of Yield Stress Fluids. Study of an Aqueous Gel. *J. Non-Newtonian Fluid Mech*. 1990; 36: 85-108.

Mckenna SP, Mcgillis WR. Performance of Digital Image Velocimetry Processing Techniques. *Exp. Fluids*. 2002; 32:106-115.

Melling A. Tracer particles and seeding for particle image Velocimetry. *Meas. Sci. Technol*. 1997; 8(12): 1406–1416.

Metzner AB, Otto RE. Agitation of Non-Newtonian Fluids. *AIChE Journal.*1957; 3: 3-10

Pakzad L, Ein-mozaffari F, Chan P. Analysis of Cavern Formation in Mixing of Yield Stress Fluids Using Tomography and CFD Modeling. *Sixth International Symposium on Mixing in Industrial Process Industries - ISMIP VI*. 2008: 1-2.

Park YS, Liu PL. Oscillatory pipe flows of a yield-stress fluid. *J. Fluid Mech*. 2010; 658: 211–228.

Paul EL, Atiemo-Obeng VA, Kresta SM. *Handbook of Industrial Mixing*. Hoboken, NJ: Wiley-Interscience, 2004.

Piau JM. carbopol Gels: Elastoviscoplastic and Slippery Glasses Made of Individual Swollen Sponges Meso- and Macroscopic Properties, Constitutive Equations and Scaling Laws. *J. Non-Newtonian Fluid Mech*. 2007; 144(1): 1-29.

Prasad AK. Particle Image Velocimetry. *Curr. Sci*. 2000 ; 79(1) : 51-60.

Reed CS. Selecting the Right Equipment for Agitation and Blending, Part 3. *Tappi Journal*. 1995:248-250.

Renaud E, Line A. Radially Agitated Tank. *AIChE Journal.* 2003; 49(3): 585-603.

Rewatkar VB, Joshi JB. Effect of Impeller Design on Liquid Phase Mixing in Mechanically Agitated Reactors. *Chem. Eng. Commun.* 1991; 102(1): 1-33.

Roberts GP, Barnes HA. New Measurements of the Flow-curves for carbopol Dispersions without Slip Artefacts. *Rheologica Acta*. 2001; 40(5): 499-503.

Saeed S, Ein-mozaffari F, Upreti SR. Using Computational Fluid Dynamics To Study the Dynamic Behavior of the Continuous Mixing of Herschel-Bulkley Fluids. *Ind. Eng. Chem. Res.* 2008; 47: 7465-7475.

Scarano F, Riethmuller ML. Iterative Multigrid Approach in PIV Image Processing with Discrete Window Offset. *Exp. Fluids.* 1999; 26(6):513-523.

Sharp KV, Adrian RJ. PIV study of small-scale flow structure around a Rushton turbine. *AIChE Journal.* 2001; 47(4): 766-778.

Sheng J, Meng H, Fox RO. Validation of CFD simulations of a stirred tank using Particle Image Velocimetry Data. *Can. J. Chem. Eng.* 1998; 76: 611-625.

Sheridan J, Wu J, Pullum L. Non-Newtonian Flow over the Trailing Edge of an Airfoil. *Exp. Therm. Fluid Sci.* 1996; 12: 244-249.

Steffe JF. *Rheological Methods in Food Process Engineering,* Second edition. East Lansing, MI: Freeman Press, 1996: 158-250.

Thakur R, Vial Ch, Djelveh G, Labbafi M. Mixing of complex fluids with flat bladed Impellers: effect of impeller geometry and highly shear-thinning behaviour. *Chem. Eng. and Process.* 2004; 43(10): 1211-1222

Torre J, Fletcher D, Lasuye T, Xuereb C. Single and Multiphase CFD Approaches for Modelling Partially Baffled Stirred Vessels: Comparison of Experimental Data with Numerical Predictions. *Chem. Eng. Sci.* 2007; 62(22): 6246-6262.

Tokpavi DL, Jay P, Magnin A, Jossic L. Experimental study of the very slow flow of a yield stress fluid around a circular cylinder. *J. Non-Newtonian Fluid Mech*. 2009; 164: 35-44

Wilkens RJ, Miller JD, Plummer JR, Dietz DC, Myers KJ. New techniques for measuring and modeling cavern dimensions in a Bingham plastic fluid. *Chem. Eng. Sci.* 2005; 60(19): 5269-5275.

Yackel DC. Pulp and Paper Agitation: The History, Mechanics, and Process. *TAPPI Press* Atlanta. 1990.

Zalc JM, Alvarez MM, Muzzio FJ, Arik BE. Extensive Validation of Computed laminar Flow in a Stirred Tank with Three Rushton Turbines. *AIChE Journal*. 2001; 47(10):2144-2154.

Zalc JM, Szalai ES, Alvarez MM, Muzzio FJ. Using CFD to understand chaotic mixing in laminar stirred tanks. *AIChE Journal.* 2002 ; 48(10) :124-2134.

Appendices

Appendix A: Mesh structure

An illustration of the mesh used in the CFD model is presented in Figure A1. The flow domain was divided into three cylinders for the meshing process. The cylinder enclosing the impeller and the bottom half of the tank were meshed using an unstructured mesh of tetrahedral elements. The top half of the tank was meshed with hexahedral elements. A high-density mesh around the impeller was used to accurately capture the gradients generated by the impeller rotation.

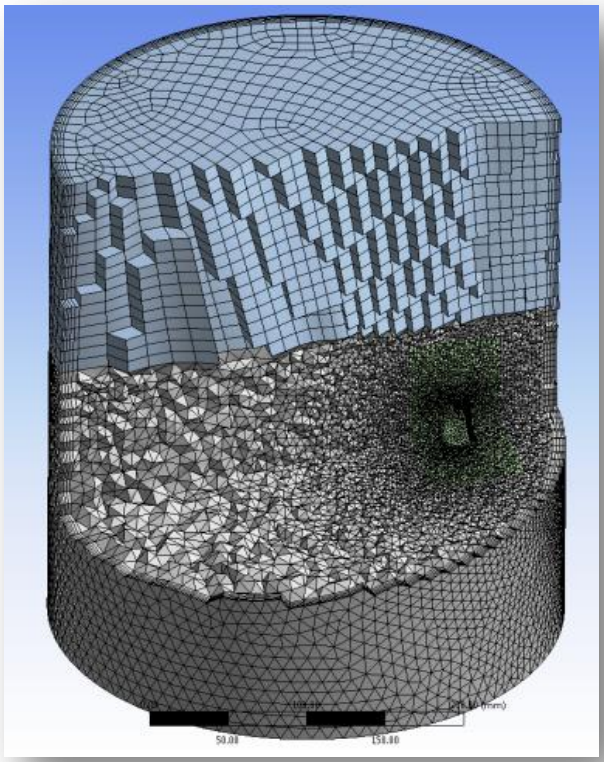

Figure A 1. Mesh structure

Appendix B: Test for grid independence.

Figure B1 shows the U and V velocities computed with 3 different grids for a specific set of conditions. The similarity of the profiles for the two grids with the higher number of elements confirms the grid independence. Similar results were obtained at other locations inside the mixing domain.

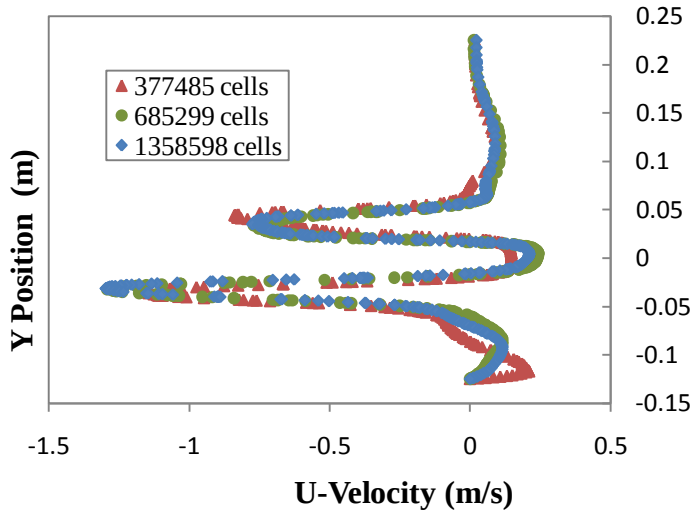

(a)

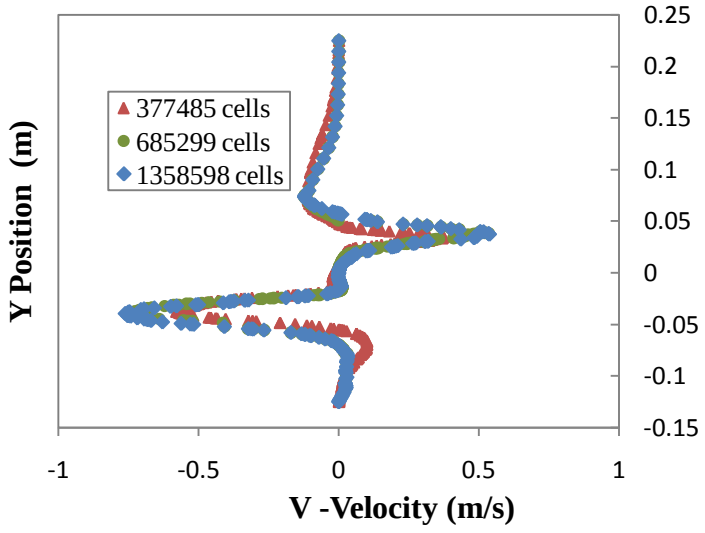

(b)

Figure B 1. Test for grid independence over a sample line located at X*=0.4 for a 0.1 w/w% carbopol solution (N= 684 rpm). (a) x-component of the velocity, (b) y-component of the velocity